JACS
JOURNAL OF THE AMERICAN CHEMICAL SOCIETY
pubs.acs.org/JACS

Article

Geometric Tuning of Coordinatively Unsaturated Copper(I) Sites in Metal–Organic Frameworks for Ambient-Temperature Hydrogen Storage

Yuto Yabuuchi, Hiroyasu Furukawa, Kurtis M. Carsch, Ryan A. Klein, Nikolay V. Tkachenko, Adrian J. Huang, Yongqiang Cheng, Keith M. Taddei, Eric Novak, Craig M. Brown, Martin Head-Gordon, and Jeffrey R. Long*

Cite This: J. Am. Chem. Soc. 2024, 146, 22759–22776

Read Online

ACCESS | Metrics & More | Article Recommendations | Supporting Information

ABSTRACT: Porous solids can accommodate and release molecular hydrogen readily, making them attractive for minimizing the energy requirements for hydrogen storage relative to physical storage systems. However, H_2 adsorption enthalpies in such materials are generally weak (−3 to −7 kJ/mol), lowering capacities at ambient temperature. Metal–organic frameworks with well-defined structures and synthetic modularity could allow for tuning adsorbent–H_2 interactions for ambient-temperature storage. Recently, $Cu_{2.2}Zn_{2.8}Cl_{1.8}(btdd)_3$ (H_2btdd = bis(1*H*-1,2,3-triazolo-[4,5-*b*],[4′,5′-*i*])dibenzo[1,4]dioxin; Cu^I-MFU-4*l*) was reported to show a large H_2 adsorption enthalpy of −32 kJ/mol owing to π-backbonding from Cu^I to H_2, exceeding the optimal binding strength for ambient-temperature storage (−15 to −25 kJ/mol). Toward realizing optimal H_2 binding, we sought to modulate the π-backbonding interactions by tuning the pyramidal geometry of the trigonal Cu^I sites. A series of isostructural frameworks, $Cu_{2.7}M_{2.3}X_{1.3}(btdd)_3$ (M = Mn, Cd; X = Cl, I; Cu^IM-MFU-4*l*), was synthesized through postsynthetic modification of the corresponding materials $M_5X_4(btdd)_3$ (M = Mn, Cd; X = CH_3CO_2, I). This strategy adjusts the H_2 adsorption enthalpy at the Cu^I sites according to the ionic radius of the central metal ion of the pentanuclear cluster node, leading to −33 kJ/mol for M = Zn^{II} (0.74 Å), −27 kJ/mol for M = Mn^{II} (0.83 Å), and −23 kJ/mol for M = Cd^{II} (0.95 Å). Thus, Cu^ICd-MFU-4*l* provides a second, more stable example of optimal H_2 binding energy for ambient-temperature storage among reported metal–organic frameworks. Structural, computational, and spectroscopic studies indicate that a larger central metal planarizes trigonal Cu^I sites, weakening the π-backbonding to H_2.

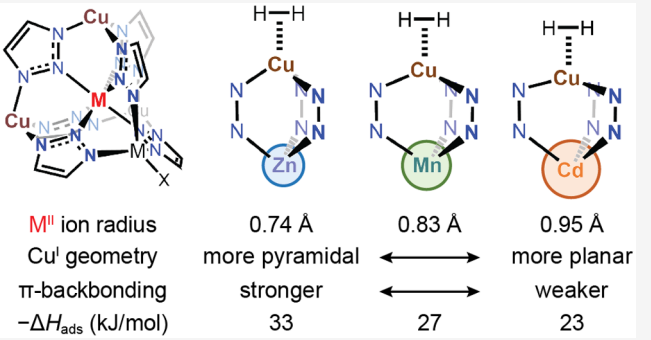

INTRODUCTION

Hydrogen is an important clean energy carrier for decarbonization due to the absence of carbon dioxide emissions upon combustion or use in a fuel cell. Although the dominant H_2 production technologies use fossil fuels or hydrocarbons, the development of renewable-energy-based technologies using ubiquitous feedstocks, such as water or biomass, would realize sustainable, net-low-, or even net-zero-emission systems.[1,2] The H_2 generated then needs to be transported to and stored at the point of use. Hydrogen is currently stored via compression or liquefaction, but extreme storage conditions (>350 bar for compression or 20 K for liquefaction) incur safety concerns as well as high capital and operation costs.[3] Instead, materials-based storage systems, such as porous adsorbents,[4] metal hydrides,[5] and organic H_2 carriers,[6] are expected to enable H_2 storage under milder conditions to realize safer and more efficient systems.[7] The nondissociative H_2 storage mechanism associated with porous adsorbents makes them particularly promising for point-of-use applications, because such storage systems necessitate high cyclability and facile H_2 charge/discharge kinetics with minimum energetic inputs.

Metal–organic frameworks (MOFs) are emergent adsorbents with pore structures and functionalities that can be tuned through the deliberate choice of metal and organic linker to optimize adsorption properties.[8,9] Such synthetic tunability is distinct from classical porous adsorbents such as zeolites and activated carbons. Indeed, early investigations on MOFs for applications in H_2 storage demonstrated that frameworks with high surface areas exhibit remarkable gravimetric H_2 capacities

Received: June 13, 2024
Revised: July 18, 2024
Accepted: July 19, 2024
Published: August 2, 2024

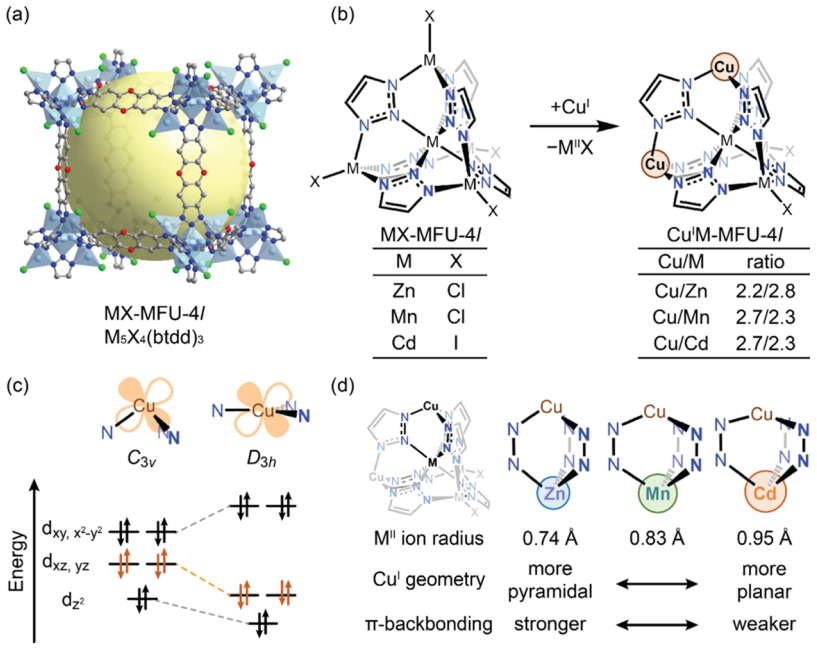

Figure 1. Schematic representation of our strategy to alter the π-basicity of open Cu^I sites in Cu^IM-MFU-4*l* frameworks by geometric tuning. The structure of MFU-4*l*-type frameworks (a) and the pentanuclear secondary building unit (b) are shown with a reaction scheme of postsynthetic metal-exchange for the secondary building unit (b). A qualitative Walsh diagram to depict the change in the energy levels of d orbitals from trigonal pyramidal geometry to trigonal planar geometry (c). Panel (d) illustrates the systematic change in the geometry of open Cu^I sites by the ionic radius of the central metal site of the pentanuclear secondary building unit. Brown, blue, gray, light blue, and light green spheres represent Cu, N, C, Zn, and Cl atoms, respectively. Hydrogen atoms are omitted for clarity. The large yellow sphere in panel (a) illustrates voids in the framework.

at 80 bar or higher, albeit at cryogenic temperatures.[10−13] Unfortunately, the adsorption capacity at ambient temperatures drops to one-third of the capacity at cryogenic conditions in most cases. Hydrogen storage at ambient temperatures by porous adsorbents is challenged by weak van der Waals interactions between H_2 and the adsorbent surface. These interactions are typically within a range of −3 to −7 kJ/mol due to the low polarizability of the H_2 molecule.[14]

Although stronger framework−H_2 interactions usually increase the adsorption capacity of H_2 at ambient temperature, extremely strong interactions may reduce the usable H_2 capacity. The usable H_2 capacity is defined as the difference in H_2 uptake between the H_2 charging and discharging conditions. The H_2 discharging pressure is proposed to be 2−5 bar to create a pressure gradient to feed H_2 from the higher-pressure storage tank to the fuel cells.[4,15] The optimal binding strength that can maximize the usable capacity was originally estimated with a single-site Langmuir adsorption model for simplicity, where the difference in the surface coverage of H_2 at the storage and discharge conditions was calculated as a function of the Gibbs free energy of adsorption to find the maximum value. This simple model for economically viable operating conditions (100−170 bar storage and 2−5 bar discharge at (sub)ambient temperatures of 223−298 K)[16] suggests that the optimal binding enthalpy is in the range of −15 to −25 kJ/mol with either the adsorption entropy assumed to be approximately −8*R* or an empirical positive correlation between enthalpy and entropy.[4,15,17,18] Note that according to this calculation, the optimal adsorption enthalpy is averaged across the entire adsorbent, which is assumed to have a homogeneous surface and obey a single-site Langmuir model. Due to the inherently weak framework−H_2 interactions, the primary focus of research has been to increase the magnitude of adsorption enthalpy. Unfortunately, obtaining binding enthalpies stronger than −10 kJ/mol has proven difficult when utilizing strategies such as linker functionalization,[19−21] formation of interpenetrated frameworks,[19] and postsynthetic metalation of frameworks.[22]

Since the first demonstration of increased H_2 uptake in a MOF by creating coordinatively unsaturated metal sites (open metal sites),[23] we and others have synthesized a variety of MOFs with open metal sites to identify critical factors in strengthening metal−H_2 interactions.[24−30] Indeed, the strength of the metal−H_2 interaction at Lewis acidic metal sites mostly follows the Irving−Williams series (Mn^{II} < Fe^{II} < Co^{II} < Ni^{II}), which is often used to explain stability constants of high-spin octahedral transition metal complexes.[27,31] Among the Ni^{II}-based frameworks, Ni_2(*m*-dobdc) (*m*-dobdc^{4-} = 4,6-dioxido-1,3-benzenedicarboxylate) has a high density of charge-dense Ni^{II} sites, achieving a record-high volumetric H_2 adsorption capacity at (sub)ambient temperatures of 223−298 K and 100 bar.[32] However, most MOFs with Lewis acidic open metal sites, including Ni_2(*m*-dobdc), still do not reach the optimal H_2 binding strength and struggle with minimal tunability of H_2 adsorption enthalpy. In particular, even upon changing the identity of metal ions,[25] functionality of the organic linker,[27,29] and/or the coordination environment of the first coordination sphere,[26,30] differences in adsorption enthalpy of less than 5 kJ/mol are observed in most cases.

Recently, coordinatively unsaturated square pyramidal V^{II} sites in the triazolate-based framework $V_2Cl_{2.8}$(btdd) (H_2btdd = bis(1*H*-1,2,3-triazolo-[4,5-*b*],[4′,5′-*i*])dibenzo[1,4]dioxin) were shown to adsorb π-acidic small molecules such as N_2 and H_2 via favorable orbital interactions, leading to much stronger gas adsorption enthalpies than classical Lewis acidic metal sites.[33−35] Notably, $V_2Cl_{2.8}$(btdd) is the first example of a porous material within the optimal H_2 binding range, exhibiting an adsorption enthalpy of −21 kJ/mol at its V^{II}

https://doi.org/10.1021/jacs.4c08039
J. Am. Chem. Soc. 2024, 146, 22759−22776

sites.[35] While $V_2Cl_{2.8}$(btdd) demonstrates the importance of orbital-interaction-mediated H_2 binding to enhance H_2 binding strength, the V^{II} sites are highly susceptible to irreversible oxidation by trace O_2. Moreover, the synthesis of analogous V^{II} frameworks, such as V_2X_2(bbta) (H_2bbta = 1*H*,5*H*-benzo(1,2-*d*:4,5-d′)bistriazole)[36,37] or V_2(dobdc) (dobdc^{4-} = 2,5-dioxido-1,4-benzenedicarboxylate)[24,38,39] has not yet been reported.

While open metal sites in MOFs capable of engaging in strong orbital interactions with H_2 are rare, the trigonal pyramidal Cu^I sites in Cu^I-MFU-4*l* ($Cu_{2.2}Zn_{2.8}(Cl/O_2CH)_{1.8}(btdd)_3$) have been reported to exhibit an excessively strong H_2 adsorption enthalpy of −32 kJ/mol.[40] The electron rich d^{10} configuration of Cu^I with a C_{3v} trigonal pyramidal geometry results in high-lying occupied d_{yz} and d_{xz} orbitals suitable for π-backbonding with H_2.[41] We note that Cu^I-MFU-4*l* is the only example of a material that exhibits strong H_2 binding up to near stoichiometric H_2 loading per Cu, although other Cu^I-based frameworks have been reported with different Cu^I coordination geometries.[42−44] The significance in the geometry for π-backbonding by trigonal Cu^I sites can be rationalized by the energy level of the π-symmetric d_{yz} and d_{xz} orbitals with ligand field theory. While the trigonal pyramidal geometry (C_{3v} symmetry) results in high-lying d_{yz} and d_{xz} orbitals because of antibonding interactions with the σ-donating ligand orbitals, a trigonal planar geometry (D_{3h} symmetry) affords lower-lying d_{yz} and d_{xz} orbitals because of the reduced spatial overlap with ligand orbitals.[41,45] The lower-lying d_{yz} and d_{xz} orbitals of trigonal planar Cu^I sites have a less favorable energy match with the σ_u* orbital of the H_2 molecule, thus minimizing π-backbonding to H_2.

This hypothesis prompted us to design trigonal Cu^I sites with an increased degree of planarity to modulate the strength of π-backbonding at the Cu^I site. More specifically, while Cu^I-MFU-4*l* has an octahedral Zn^{II} ion at the center of the pentanuclear secondary building units, we hypothesized that replacing this central ion with larger metal ions could expand the tripodal ligand scaffold, thereby making the peripheral Cu^I ion protrude less from the tripodal ligand scaffold to increase its planarity (Figure 1). Here, we establish a series of Cu^IM-MFU-4*l* frameworks (M = Zn, Mn, Cd; hereafter, the previously reported Cu^I-MFU-4*l* will be denoted as Cu^IZn-MFU-4*l*) with different M^{II} ions at the center of the pentanuclear cluster node (Figure 1). Using *in situ* spectroscopy, computational studies, diffraction studies, and gas adsorption measurements, we demonstrate that H_2 binding in this series can be systematically tuned, allowing the realization of new materials within the optimal range for ambient-temperature hydrogen storage.

EXPERIMENTAL SECTION

Detailed synthetic and characterization procedures are provided in the Supporting Information (SI). The compounds H_2btdd, $Zn_5Cl_4(btdd)_3$ (ZnCl-MFU-4*l*), and $Cu_{2.2}Zn_{2.8}Cl_{1.8}(btdd)_3$ (Cu^IZn-MFU-4*l*) were synthesized using a previously reported procedure.[41,46] Unless noted, reactions were performed in an N_2 atmosphere in a glovebox with deoxygenated anhydrous solvent.

Synthesis of $Mn_5(CH_3CO_2)_4(btdd)_3$ (Mn(OAc)-MFU-4*l*; OAc = CH_3CO_2). A 500 mL storage Schlenk flask was charged with H_2btdd (0.300 g, 1.13 mmol, 1.00 equiv), *N*,*N*-dimethylformamidium trifluoromethanesulfonate (1.26 g, 5.63 mmol, 5.00 equiv), and 130 mL of *N*,*N*-dimethylformamide (DMF). A solution of anhydrous manganese acetate (0.331 g, 1.92 mmol, 1.70 equiv) in 20 mL of methanol was then added to the beige suspension. The flask was sealed, and the mixture was stirred at 125 °C for 7 days, during which a fine beige powder precipitated. This powder was collected by filtration over a fine porosity frit and subsequently suspended in ∼15 mL of DMF and heated at 120 °C for 4 h. The supernatant was subsequently decanted and replaced with ∼15 mL of fresh DMF five times. Additional solvent exchanges were then performed with ∼15 mL of methanol at 60 °C four times, followed by ∼10 mL of dichloromethane at room temperature twice. The dichloromethane-solvated material was subsequently activated under dynamic vacuum at 180 °C for 24 h to afford 0.417 g (85%) of product as a microcrystalline beige solid. Elemental analysis calcd for $Mn_5(CH_3CO_2)_4(C_{12}H_4O_2N_6)_3$: C, 40.54%; H, 1.86%, N, 19.34%. Found: C, 41.19%; H, 1.44%; N, 17.51%.

Synthesis of $Mn_5Cl_4(btdd)_3$ (MnCl-MFU-4*l*). Desolvated Mn(OAc)-MFU-4*l* (0.060 g, 0.046 mmol, 1.0 equiv) was suspended in a solution of calcium chloride (0.10 g, 0.92 mmol, 20 equiv) in 15 mL of methanol at room temperature for 1 day. The supernatant was decanted, and the residual solid was suspended in a fresh second solution of calcium chloride (0.10 g, 0.92 mmol, 20 equiv) in 15 mL of methanol again at room temperature for another day. The product was washed with ∼15 mL of methanol at room temperature for 3 h four times. The resultant beige powder was activated under dynamic vacuum at 180 °C for 24 h to afford 0.053 g (95%) of product as a microcrystalline beige solid or used directly in the subsequent metal exchange reaction. Elemental analysis calcd for desolvated $Mn_5Cl_4(C_{12}H_4O_2N_6)_3$: C, 36.75%; H, 1.00%; N, 20.85%. Found: C, 37.05%; H, 1.07%; N, 20.54%.

Synthesis of $Cu_{2.7}Mn_{2.3}Cl_{1.3}(btdd)_3$ (Cu^IMn-MFU-4*l*). The methanol-solvated MnCl-MFU-4*l* from the above procedure was subsequently used without isolation of MnCl-MFU-4*l*. Solvent exchange for the methanol-solvated MnCl-MFU-4*l* was performed with ∼10 mL of acetonitrile at room temperature three times over 1 day. After the bulk of acetonitrile was decanted, the acetonitrile-solvated MnCl-MFU-4*l* was suspended in a solution of copper(I) chloride dimethylsulfide (0.15 g, 0.92 mmol, 20 equiv) in ∼15 mL of acetonitrile at 60 °C for 1 day. The supernatant was decanted, and the residual solid was suspended in a second fresh solution of copper(I) chloride dimethylsulfide (0.15 g, 0.92 mmol, 20 equiv) in ∼15 mL of acetonitrile at 60 °C for another day. The beige solids were suspended with ∼15 mL of acetonitrile at room temperature twice, with ∼15 mL of acetonitrile at 60 °C once, and with ∼10 mL of methanol at room temperature three times. The beige powder was collected by filtration and then activated under dynamic vacuum at 90 °C for 12 h, then heated at 200 °C for 48 h to afford 0.044 g (85% based on the starting Mn(OAc)-MFU-4*l* material) of product as a microcrystalline beige solid. Elemental analysis calcd for $Mn_{2.3}Cu_{2.7}Cl_{1.3}(C_{12}H_4O_2N_6)_3$: C, 38.04%; H, 1.06%; N, 22.18%. Found: 34.15%; H, 1.16%; N, 17.84%. The slightly lower carbon and nitrogen ratios may indicate the presence of extra copper at defect sites and/or in the pore.

Synthesis of $Cd_5I_4(btdd)_3$ (CdI-MFU-4*l*). This reaction was performed on a benchtop under air. Solvent was used as received without purification. A homogeneous solution of H_2btdd (0.500 g, 1.88 mmol, 1.00 equiv) in 400 mL of DMF and a homogeneous solution of CdI_2 (13.8 g, 37.6 mmol, 20.0 equiv) in 100 mL of DMF (100 mL) was charged in a 1 L round-bottom flask, and the mixture was heated with stirring at 145 °C for 7 days. The beige powder was collected by filtration and washed with ∼40 mL of fresh DMF at 120 °C for 6 h ten times. Solvent exchange was performed with methanol via Soxhlet extraction for 5 days. The methanol-solvated material was activated under dynamic vacuum at 120 °C for 24 h to afford 0.704 g (60%) of product as a microcrystalline beige solid. Elemental analysis calcd for $Cd_5I_4(C_{12}H_4O_2N_6)_3$: C, 23.22%; H, 0.65%; N, 13.54%. Found: C, 27.99%; H, 1.09%; N, 13.99%. The slightly higher carbon, hydrogen, and nitrogen ratios may indicate the presence of residual organic guests that were not fully removed by activation.

Synthesis of $Cu_{2.7}Cd_{2.3}I_{1.3}(btdd)_3$ (Cu^ICd-MFU-4*l*). Desolvated CdI-MFU-4*l* (0.150 g, 0.0805 mmol) was suspended in a solution of copper(I) iodide (0.153 g, 0.805 mmol, 10.0 equiv) in 20 mL of acetonitrile at 60 °C for 24 h. The supernatant was decanted, and the remaining brown powder was washed with ∼20 mL of fresh

https://doi.org/10.1021/jacs.4c08039
J. Am. Chem. Soc. 2024, 146, 22759−22776

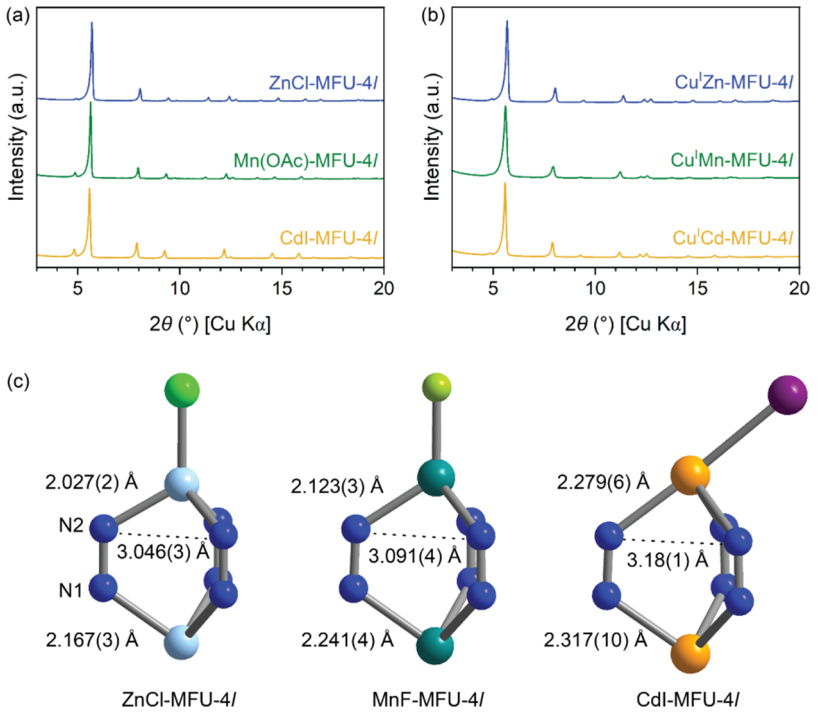

Figure 2. Powder X-ray diffraction patterns of MX-MFU-4*l* (a) and Cu^{I}M-MFU-4*l* (b) collected at 298 K by Cu Kα radiation. Comparison of geometry of the tripodal ligand scaffold for a peripheral tetrahedral M ion for MX-MFU-4*l* determined by single-crystal X-ray diffraction measurements (c). Blue, light blue, light green, emerald green, yellow green, yellow, and purple spheres represent N, Zn, Cl, Mn, F, Cd, and I atoms, respectively.

acetonitrile at 60 °C for 6 h ten times. The brown powder was collected by filtration, and was activated under dynamic vacuum at 150 °C for 48 h to afford 0.123 g (92%) of product as a microcrystalline pale brown solid. Elemental analysis calcd for $Cu_{2.7}Cd_{2.3}I_{1.3}(C_{12}H_4O_2N_6)_3$: C, 31.20%; H, 0.90%; N, 18.20%. Found: C, 30.96%; H, 1.10%; N, 16.83%.

RESULTS AND DISCUSSION

The metal−organic framework $Zn_5Cl_4(btdd)_3$ (ZnCl-MFU-4*l*, previously referred to as MFU-4*l*) consists of pentanuclear zinc clusters connected by linear bisbenzotriazolate linkers ($btdd^{2-}$) to form a highly porous cubic network structure (Figure 1a). Each pentanuclear cluster has one octahedral zinc site at the center and four pseudotetrahedral zinc sites that are capped by terminal chloride anions and exposed to the pore of the framework. A variety of postsynthetic metal exchanges and anion exchanges at the peripheral sites have been reported for ZnCl-MFU-4*l* and related frameworks,[47,48] allowing for control over gas adsorption and catalysis properties.[49,50] Nonetheless, to the best of our knowledge, no studies have aimed to change the identity of the central metal site to alter properties of the peripheral metal sites. This is possibly because the central metal site is inaccessible within the cluster, prohibiting postsynthetic metal-exchange in MFU-4*l*.[51] The inaccessibility of the central metal for postsynthetic metal-exchange may lead to the incorrect assumption that the central metal does not significantly impact the surface properties of these materials.

Synthesis and Structural Characterization of MX-MFU-4*l* and Cu^{I}M-MFU-4*l* with M = Zn, Mn, Cd. We hypothesized that the central metal ion of the cluster of an MFU-4*l* framework could govern the opening of the tripodal scaffold for the peripheral sites according to the magnitude of its ionic radius, thereby adjusting the geometry of the peripheral sites and tuning their adsorption properties (Figure 1d). To synthesize MFU-4*l* frameworks with a central metal ion other than zinc(II), we conducted solvothermal syntheses using manganese(II) and cadmium(II) salts. These metals were selected because high-spin d^5 Mn^{II} and d^{10} Cd^{II} are not subject to a Jahn−Teller distortion and are therefore suitable to reside at the six-coordinate central site with an ideal octahedral geometry. Additionally, the ionic radii of Zn^{II} (0.74 Å), high-spin Mn^{II} (0.83 Å) and Cd^{II} (0.95 Å) are almost evenly spaced with an approximately 0.1 Å difference,[52] allowing for systematic structure−property examinations.

Solvothermal reaction of H_2btdd with $Mn(OAc)_2$ (OAc = CH_3CO_2) in DMF/CH_3OH (6.5/1 *v*/*v*) or CdI_2 in DMF yielded microcrystalline powders of the cubic MFU-4*l*-type framework, which we respectively name Mn(OAc)-MFU-4*l* and CdI-MFU-4*l*. Empirically, we found that the choice of metal salt and reaction conditions is critical to obtain the MFU-4*l* phase exclusively, avoiding the formation of the hexagonal $M_2X_2(btdd)$ phase and other phases.[34,53,54]

Powder X-ray diffraction patterns of activated Mn(OAc)-MFU-4*l* and CdI-MFU-4*l* are nearly identical to that of ZnCl-MFU-4*l*, indicating the structural similarity of these frameworks (Figure 2a). As metal ionic radius increases from Zn^{II} to Mn^{II} to Cd^{II}, the peak positions shift to lower angles such that the unit cell parameter *a* increases along the series ZnCl-MFU-4*l* < Mn(OAc)-MFU-4*l* < CdI-MFU-4*l*. For example, the most intense peak, corresponding to the (200) plane, is observed with Cu Kα at 2θ = 5.70, 5.64, and 5.58° for ZnCl-MFU-4*l*, Mn(OAc)-MFU-4*l*, and CdI-MFU-4*l*, respectively, at room temperature. The robustness of the crystal structures after activation is also supported by N_2 adsorption data collected at 77 K. The materials show steep N_2 uptake below P/P_0 = 0.1, reaching capacities of more than 25 mmol/g and demonstrating the presence of permanent porosity. From these data, the

https://doi.org/10.1021/jacs.4c08039
J. Am. Chem. Soc. 2024, 146, 22759−22776

Table 1. Comparison of Surface Areas, Pore Volumes, Unit Cell Parameters, and Isosteric Enthalpies of H_2 Adsorption for MX-MFU-4*l* and Cu^IM-MFU-4*l* Compounds

		surface area (m^2/g)			pore volume (cm^3/g)			
material	formula	BET	Langmuir	Langmuir (calcd.)[a]	DR (obsd.)[b]	calcd.[a]	*a* (Å)[c]	$-\Delta H_{ads}$ (kJ/mol)[d]
ZnCl-MFU-4*l*	$Zn_5Cl_4(btdd)_3$	3470(30)	3880(10)	3990	1.38	1.42	31.0736(5)	6.5
Mn(OAc)-MFU-4*l*	$Mn_5(OAc)_4(btdd)_3$	3180(20)	3520(10)	3870	1.25	1.37	31.4217(2)	6.5
MnCl-MFU-4*l*	$Mn_5Cl_4(btdd)_3$	3430(20)	3800(10)	4260	1.35	1.51	31.2844(6)	6.6
CdI-MFU-4*l*	$Cd_5I_4(btdd)_3$	2480(20)	2750(10)	2830	0.977	1.01	31.5615(5)	6.4
Cu^IZn-MFU-4*l*	$Cu_{2.2}Zn_{2.8}Cl_{1.8}(btdd)_3$	3660(60)	4080(10)	4470	1.45	1.59	31.1286(5)	33.4 [32][40]
Cu^IMn-MFU-4*l*	$Cu_{2.7}Mn_{2.3}Cl_{1.3}(btdd)_3$	3000(20)	3340(10)	4930	1.19	1.76	31.5076(6)	26.9
Cu^ICd-MFU-4*l*	$Cu_{2.7}Cd_{2.3}I_{1.3}(btdd)_3$	2930(20)	3280(10)	3940	1.18	1.40	31.6372(10)	22.7

[a]Calculated based on the available free volume with the Connolly method for a model structure. [b]Pore volume estimated by the Dubinin–Radushkevich method. [c]Cubic unit cell parameter obtained by Pawley fit for a powder X-ray diffraction pattern at 298 K. [d]Isosteric enthalpy of H_2 adsorption estimated by the Clausius–Clapeyron equation for the H_2 loading at 0.50 mmol/g.

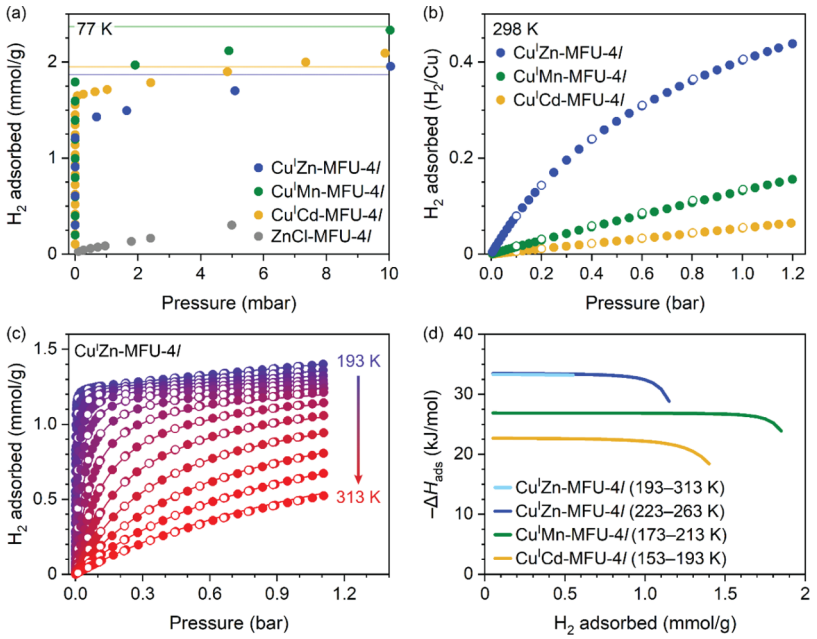

Figure 3. H_2 adsorption isotherms for ZnCl-MFU-4*l* (gray), Cu^IZn-MFU-4*l* (blue), Cu^IMn-MFU-4*l* (green), and Cu^ICd-MFU-4*l* (yellow) at 77 K (a) and 298 K (b). Blue, green, and yellow horizontal lines in panel (a) represent expected H_2 uptake for one H_2 per Cu^I based on the chemical formula of $Cu^I_{2.2}Zn_{2.8}Cl_{1.8}(btdd)_3$, $Cu^I_{2.7}Mn_{2.3}Cl_{1.3}(btdd)_3$, and $Cu^I_{2.7}Cd_{2.3}I_{1.3}(btdd)_3$, respectively. H_2 adsorption isotherms of Cu^IZn-MFU-4*l* from 193 to 313 K collected in 10 K intervals (c). Filled and open circles represent adsorption and desorption data, respectively. Solid lines represent fit to a dual-site Langmuir–Freundlich equation for the analyzed temperature range. Isosteric enthalpy of H_2 adsorption for Cu^IM-MFU-4*l* frameworks (d).

Brunauer–Emmett–Teller (BET) surface areas are estimated to be 3180(20) m^2/g for Mn(OAc)-MFU-4*l* and 2480(20) for CdI-MFU-4*l* (Table 1). The lower surface areas of Mn(OAc)-MFU-4*l* and CdI-MFU-4*l* compared to ZnCl-MFU-4*l* are attributed to the larger capping anions at the peripheral metal sites of the pentanuclear clusters, as well as the greater atomic masses of Cd and iodine for CdI-MFU-4*l*. Indeed, the pore volumes of both Mn(OAc)-MFU-4*l* and CdI-MFU-4*l* by the Dubinin–Radushkevich method[55] (V_p) agree within 10% of the calculated values (V_{calcd}) expected from the available free volume of the structures, as modeled using Materials Studio (Table 1).[56]

Successful syntheses of MX-MFU-4*l* frameworks prompted us to diagnose how the metal identity affects structural parameters, specifically unit cell parameters and the local geometry of the pentanuclear cluster. We therefore screened synthetic conditions for growing single crystals of MX-MFU-4*l*. Treatment of H_2btdd with MnI_2 in a DMF/CH_3OH/HNO_3 mixture followed by postsynthetic anion exchange with F^- afforded single crystals of MnF-MFU-4*l* (see SI for experimental details; treatment with fluoride was implemented to resolve the anion compositional disorder present from the solvothermal synthesis). For CdI-MFU-4*l*, crystals were grown with a condition similar to that reported for ZnCl-MFU-4*l*.[57]

All MX-MFU-4*l* frameworks crystallize in the cubic space group $Fm\bar{3}m$ with slightly different unit cell parameters of a = 30.9085(3) Å for ZnCl-MFU-4*l*, 30.9027(9) Å for MnF-MFU-4*l*, and 31.1633(6) Å for CdI-MFU-4*l* at 100 K (Table S9). Interestingly, the ionic radius of the central metal M is not reflected in the trend of these unit cell parameters. Furthermore, the unit cell parameters determined for the single crystals are smaller than those obtained for microcrystalline powders by Pawley fits against the powder X-ray diffraction data, even when considering the difference in temperature for these experiments (100 and 298 K for single-crystal X-ray diffraction and powder X-ray diffraction,

https://doi.org/10.1021/jacs.4c08039
J. Am. Chem. Soc. 2024, 146, 22759–22776

respectively). We note that the $btdd^{2-}$ linker is not strictly planar in the MX-MFU-4*l* crystal structures, because the dibenzodioxin moieties are generally found to be disordered over two bent positions due to thermal breathing motions (Figure S51). Particle size and temperature variations may contribute to different degrees of linker vibrations, causing the discrepancy between the unit cell parameters determined from single-crystal and powder X-ray diffraction data. In addition, the extent to which the linker can bend becomes greater for frameworks with larger metals. This linker bending, as well as the size of the capping anion, explain the slightly smaller unit cell parameter of MnF-MFU-4*l* compared to ZnCl-MFU-4*l*, although the ionic radius of Mn^{II} is larger than that of Zn^{II}. Despite the counterintuitive trend of the unit cell parameter determined by single-crystal X-ray diffraction versus the size of M^{II} ions, the geometry of a tripodal ligand scaffold reflects the size of M^{II} ions (Figure 2c). A larger central M^{II} ion forms a longer bond to the middle N1 atom of each triazolate group and a larger opening of the tripodal site for a peripheral metal site, as gauged by the distance between the closest N2 atoms of neighboring linkers.

Copper(I) was introduced into the peripheral sites of the pentanuclear clusters in each of the new MX-MFU-4*l* frameworks by postsynthetic metal-exchange using $Cu^{I}X$ salts to yield the corresponding Cu^{I}M-MFU-4*l* (M = Mn, Cd) framework materials. For Cu^{I}Mn-MFU-4*l*, anion-exchange with Cl^- for OAc^- was first performed for Mn(OAc)-MFU-4*l*, and then Cu^{I}-exchange was carried out with $Cu^{I}Cl{\cdot}S(CH_3)_2$ in acetonitrile. For Cu^{I}Cd-MFU-4*l*, Cu^{I} was incorporated into the framework using $Cu^{I}I$ in acetonitrile. Retention of crystallinity following Cu^{I} incorporation and successful removal of unreacted Cu^{I} salts was confirmed by powder X-ray diffraction analysis (Figure 2b). Inductively coupled plasma optical emission spectroscopy (ICP-OES) allowed for estimation of Cu:M ratios of the Cu^{I}-exchanged products, revealing approximately 2.7:2.3 for both Cu^{I}Mn-MFU-4*l* and Cu^{I}Cd-MFU-4*l*. The pore volume estimated by the N_2 adsorption isotherm of the Cu^{I}M-MFU-4*l* series tends to be lower than the theoretical volume by 10−30%. The slightly lower measured pore volume of the Cu^{I}M-MFU-4*l* frameworks may occur because postsynthetic metal-exchange caused small losses in structural integrity.

H_2 Adsorption Properties at Low Pressure. To examine the hydrogen adsorption properties of the MX-MFU-4*l* and Cu^{I}M-MFU-4*l* frameworks, we collected low-pressure H_2 adsorption isotherms at 77 K (Figure 3a). All parent MX-MFU-4*l* frameworks show similar adsorption profiles at 77 K, with no steep uptake below 1 mbar indicating the absence of strong H_2 adsorption sites.[58] In contrast, all Cu^{I}M-MFU-4*l* frameworks exhibit steep H_2 adsorption profiles below 1 mbar at 77 K. Notably, H_2 uptake at 77 K and 1 mbar in Cu^{I}M-MFU-4*l* reaches approximately 80% of the expected value for one H_2 per Cu^{I} site of the frameworks in each Cu^{I}M-MFU-4*l* (80, 85, and 87% for Cu^{I}Zn-MFU-4*l*, Cu^{I}Mn-MFU-4*l*, and Cu^{I}Cd-MFU-4*l*, respectively), suggesting that the initial steep H_2 uptake results from H_2 binding at the open Cu^{I} sites. The slightly lower H_2 uptake than theoretically expected implies the presence of inactive Cu for H_2, possibly present at defect sites. Since the uptake below 1 mbar at 77 K was too steep to compare the H_2 binding strengths of the frameworks, H_2 adsorption isotherms were also collected at 298 K (Figure 3b). The initial slope of the isotherms (Henry's law constant, Table S2) indicates that the H_2 binding strength ranks in the order Cu^{I}Zn-MFU-4*l* > Cu^{I}Mn-MFU-4*l* > Cu^{I}Cd-MFU-4*l*.

The isosteric enthalpy of H_2 adsorption (ΔH_{ads}, which, although discouraged,[59] is also sometimes referred to as the isosteric heat of adsorption, Q_{st}) can be calculated by collecting adsorption isotherms at multiple temperatures and applying the Clausius−Clapeyron equation.[60] Briefly, the logarithms of the pressures that give a specific adsorbed amount of H_2 at certain temperatures are plotted against reciprocal temperatures to obtain $\Delta H_{ads}/R$ as its slope, where R is the gas constant. The pressure that gives a specific gas loading at a given temperature is often determined using the Langmuir−Freundlich model. The best practice for using that Clausius−Clapeyron analysis is to use a narrow temperature range (10−40 K),[60] because a temperature-dependence of the isosteric enthalpy of adsorption can arise.[61,62] However, our experiments revealed that the H_2 binding strengths for Cu^{I}M-MFU-4*l* frameworks vary widely, prohibiting use of the same temperature range for all three frameworks in a holistic Clausius−Clapeyron analysis. We therefore decided to collect H_2 isotherms at a wide temperature range for Cu^{I}Zn-MFU-4*l*, for which ΔH_{ads} was reported to be −32 kJ/mol with 163−193 K isotherms, to examine how the ΔH_{ads} values are affected by the temperature range selected for the analysis.

The H_2 isotherms for Cu^{I}Zn-MFU-4*l* from 193 to 313 K were fitted with the Langmuir−Freundlich equation using temperature independent parameters (Figures 3c and S30). We note that the simulated isotherms generated from the resulting fit parameters match well with the corresponding experimental isotherm at these temperatures, indicating minimal temperature dependence of the thermodynamic parameters for the adsorption sites in the Langmuir−Freundlich model for the examined temperature range. Using these fit parameters, we plotted the logarithm of pressure versus reciprocal temperature (i.e., ln P vs $1/T$, a Clausius−Clapeyron plot) for various H_2 loadings with 0.05 mmol/g increments for the 193−313 K range, finding an excellent linearity with $R^2 > 0.999$ up to the highest H_2 uptake at 1 bar and 313 K (Figure S31). The Clausius−Clapeyron analysis revealed a nearly constant ΔH_{ads} value of −33.3 kJ/mol with respect to loading up to 0.6 mmol/g of H_2 uptake (light blue line in Figure 3d), similar to the reported value of −32.3 kJ/mol determined using isotherm data recorded at 163−193 K.[40] Next, we performed the same analyses for the isotherm data while dividing them into four sets with 20 K windows (203−223, 233−253, 263−283, and 293−313 K). The Clausius−Clapeyron analyses for these various temperature windows result in similar ΔH_{ads} values within ±1 kJ/mol, with the ΔH_{ads} values estimated for higher temperatures being slightly stronger (Figure S43 and Table S4). Slight increases in the magnitude of ΔH_{ads} at higher temperatures could be explained by the difference in heat capacities between the gas phase and the adsorbed phase due to switching of the translational freedom in the gas phase into the vibrational freedom in the adsorbed phase.[63]

Upon recognizing that ΔH_{ads} for H_2 adsorption onto a series of Cu^{I}M-MFU-4*l* slightly depends on temperature on the order of 2 kJ/mol in a 120 K window, we selected a different temperature window for each Cu^{I}M-MFU-4*l* framework for the Clausius−Clapeyron analysis. Specifically, to estimate ΔH_{ads} for the Cu^{I}M-MFU-4*l* frameworks, we chose a 40 K temperature range where the strong adsorption sites are not fully saturated at 0.01 bar while the uptake approaches one H_2

https://doi.org/10.1021/jacs.4c08039
J. Am. Chem. Soc. 2024, 146, 22759−22776

per Cu^I near 1 bar. The reasons for these criteria are (i) to avoid steep H_2 uptake in the low-pressure region, which may reduce the reliability of the pressure reading due to the limitation of the pressure transducer of the instrument, and (ii) to ensure appreciable H_2 capacities. With these criteria, the temperature ranges selected to calculate the ΔH_{ads} values for the Cu^IM-MFU-4*l* series were 223−263 K for Cu^IZn-MFU-4*l* (Figures S32 and S33), 173-213 K for Cu^IMn-MFU-4*l* (Figures S36 and S37), and 153−193 K for Cu^ICd-MFU-4*l* (Figures S40 and S41). Isothermal adsorption data collected at other temperatures for Cu^IMn-MFU-4*l* and Cu^ICd-MFU-4*l* that were not used for the Clausius−Clapeyron analysis are provided in the SI (Figures S34 and S38).

The Clausius−Clapeyron analysis reveals that the initial ΔH_{ads} values are −33.4, −26.9, and −22.7 kJ/mol for Cu^IZn-MFU-4*l*, Cu^IMn-MFU-4*l*, and Cu^ICd-MFU-4*l*, respectively (Figure 3d). A nearly flat $-\Delta H_{ads}$ curve was observed up to approximately 80% of the expected uptake for one H_2 per Cu^I based on the formula unit of each Cu^IM-MFU-4*l* framework. The H_2 loading when $-\Delta H_{ads}$ starts to decrease (1.2, 1.9, and 1.4 mmol/g for Cu^IZn-MFU-4*l*, Cu^IMn-MFU-4*l*, and Cu^ICd-MFU-4*l*, respectively) is reminiscent of H_2 uptake in each Cu^IM-MFU-4*l* framework at 1 mbar and 77 K (1.3, 1.9, and 1.7 mmol/g for Cu^IZn-MFU-4*l*, Cu^IMn-MFU-4*l*, and Cu^ICd-MFU-4*l*, respectively). These Clausius−Clapeyron analyses also confirm that the H_2 binding enthalpy follows the order Cu^IZn-MFU-4*l* > Cu^IMn-MFU-4*l* > Cu^ICd-MFU-4*l*, as shown in the 298-K isotherm data (Figure 3b). This order follows the trend in size of the central metal ion within each pentanuclear cluster, with larger metals giving lower binding enthalpies. Notably, ΔH_{ads} for Cu^ICd-MFU-4*l* (−22.7 kJ/mol) is in the range of the optimal binding enthalpy for ambient temperature H_2 storage (−15 to −25 kJ/mol). Thus, the material represents just the second example of a MOF that exhibits the optimal H_2 binding enthalpy.[35] We also note that, although the Cu^I-containing framework NU-2100 was recently reported to show a high initial ΔH_{ads} of −32 kJ/mol, the strong H_2 binding in this material is limited to only ∼1% of Cu^I in the framework (0.025 mmol/g), and the nature of the sites responsible has not been elucidated.[44] In contrast, the quantity of strong adsorption sites in the Cu^IM-MFU-4*l* series approaches the stoichiometric value for one H_2 per Cu^I, thereby allowing an examination of structure−property effects with well-defined Cu^I sites.

***In Situ* Gas-Dosing Infrared Spectroscopy.** To investigate the origins of the trend in ΔH_{ads} values for the Cu^IM-MFU-4*l* frameworks, we performed *in situ* H_2- and D_2-dosing infrared spectroscopy on the materials and examined the shifts in the H−H and D−D stretching frequencies upon adsorption. Each activated framework was cooled to 90 K and dosed with ∼600 mbar of D_2 and a spectrum was collected. The sample was then activated under dynamic vacuum at elevated temperature to fully desorb D_2. Subsequently, the sample was cooled to 90 K again to dose ∼600 mbar of H_2 and another spectrum was collected. The D_2-dosed spectrum was subtracted from the H_2-dosed spectrum to isolate signals for the adsorbed species while negating the change in vibrational signals of the framework due to the change in the coordination geometry of Cu^I upon gas binding (Figures S45, S47, and S49).

The difference IR spectra for the three Cu^IM-MFU-4*l* frameworks exhibit two peaks for H_2 (Figure 4). One is a broad asymmetric peak most intense at 3250, 3300, and 3380 cm^{-1} for Cu^IZn-MFU-4*l*, Cu^IMn-MFU-4*l*, and Cu^ICd-MFU-4*l*, respectively (Table 2). The other peak is sharp and lower in intensity, and is centered around 4120 cm^{-1} for all Cu^IM-MFU-4*l* frameworks. Given that the H−H stretching frequency, ν(H−H), of free H_2 arises at 4161 cm^{-1},[64] we assign the broad peaks (for which the extent of peak shift depends on the central metal identity) to the stretching mode of H_2 strongly bound to Cu^I sites, whereas we assign the peaks at ∼4120 cm^{-1} to H_2 weakly bound at secondary, nonmetal adsorption sites. The broadening of an H−H stretching signal is commonly observed for molecular H_2 complexes[65] and has also been seen previously for Cu^IZn-MFU-4*l*,[41] supporting our assignment of the signal for H_2 bound to Cu^I sites. Such peak broadening is characteristic of a chemically activated H_2 molecule, which results in a considerably broad, asymmetric probability distribution for the internuclear distance.[66] The trend in the shifts of ν(H−H) confirms that the H−H bond is less activated when bound to a Cu^I site residing at a pentanuclear secondary building unit with a larger central metal.

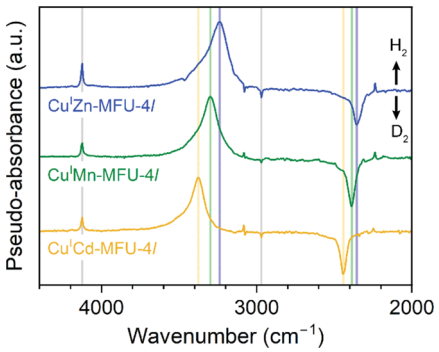

Figure 4. Difference IR spectra collected at 90 K for Cu^IZn-MFU-4*l* (blue), Cu^IMn-MFU-4*l* (green), and Cu^ICd-MFU-4*l* (yellow), where the D_2-dosed spectrum was subtracted from the H_2-dosed spectrum. The IR bands associated with H_2 adsorption appear as positive peaks whereas the IR bands associated with D_2 adsorption appear as negative peaks. The gray vertical lines highlight signals by weakly physisorbed H_2 and D_2 whereas the colored lines highlight peak maximum for H_2 and D_2 bound to Cu^I sites in each Cu^IM-MFU-4*l*.

The same trend was also observed for D_2, for which the signals appear as negative peaks in the difference spectrum (Figure 4). The peak position of the small peak for nonmetal adsorption sites is almost invariant for all Cu^IM-MFU-4*l* frameworks at ∼2970 cm^{-1}, whereas the position of the peak for D_2 strongly bound to Cu^I is located at 2360, 2390, and 2440 cm^{-1} for Cu^IZn-MFU-4*l*, Cu^IMn-MFU-4*l*, and Cu^ICd-MFU-4*l*, respectively. The ratios of the H_2:D_2 stretching frequency for the corresponding adsorption site are consistent with the change in the reduced mass between H_2 and D_2 within 3% error for both Cu^I sites and nonmetal adsorption sites.

Analysis of variable-temperature IR data in the presence of H_2 can also provide site-specific thermodynamic parameters of H_2 adsorption through use of the van't Hoff equation. However, we encountered difficulties in integrating the peak area to perform a van't Hoff analysis for H_2 adsorption in the Cu^IM-MFU-4*l* frameworks owing to (i) the broad asymmetric shape of the IR band for the chemically activated H_2 and (ii) changes in signals associated with framework vibration due to the slight change in the coordination geometry of Cu^I upon gas binding.[41] In this work and our previous work,[41] we used a D_2-

https://doi.org/10.1021/jacs.4c08039
J. Am. Chem. Soc. 2024, 146, 22759−22776

Table 2. Summary of Experimental and Computational H−H Stretching Frequency and Thermodynamic Parameters of H_2 Bound to a Cu^I Site

	ν(H−H) (cm^{-1})			$-\Delta H°$ (kJ/mol)		
materials	obsd.	calcd.[a] (anharm.)[b]	calcd. (harm.)[c]	obsd. (IR)[d]	obsd. (CC)[e]	calcd.[f]
Cu^IZn-MFU-4*l*	3250	3251	3582	29.4(2)	33.4	31.6
Cu^IMn-MFU-4*l*	3300	3317	3638	23.6(2)	26.9	26.7
Cu^ICd-MFU-4*l*	3380	3356	3665	17.7(2)	22.7	24.1

[a]Obtained by DFT calculation at the B3LYP-D3BJ/def2-SVP level theory. [b]Obtained with anharmonic corrections. [c]Obtained without anharmonic corrections. [d]The errors represent the uncertainty originating from the least-squares regression analysis in a van't Hoff linear plot. [e]Obtained by a Clausius−Clapeyron (CC) analysis for the H_2 loading of 0.50 mmol/g as shown in Figure 3. [f]Obtained by DFT calculations at the ωB97M-V/def2-TZVPPD//B3LYP-D3BJ/def2-SVP level theory.

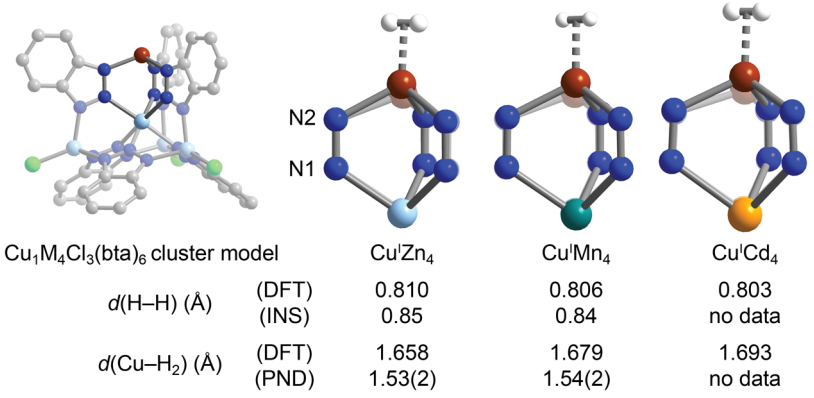

Figure 5. (Left) DFT-optimized structure of the $Cu_1Zn_4Cl_3(bta)_6$ cluster. (Right) DFT-optimized geometry for the open Cu^I site binding an H_2 molecule. DFT-optimized geometry without an H_2 molecule is shown as a faded illustration to visualize Cu^I pyramidalization upon H_2 binding. The H−H distance estimated by inelastic neutron scattering (INS) spectroscopy and the Cu−D_2 distance refined by powder neutron diffraction (PND) are shown for comparison. White, blue, gray, light blue, light green, emerald green, and yellow spheres represent H, N, C, Zn, Cl, Mn, and Cd atoms, respectively. Hydrogen atoms on the bta^- ligand are omitted for clarity.

Table 3. Structural Parameters of Cu^IM-MFU-4*l* from DFT Calculation, Powder Synchrotron X-ray Diffraction (PSXRD), and Powder Neutron Diffraction (PND)

	d(Cu−N2 plane) (Å)			∠M−Cu−N2 (°)		
materials[a]	DFT	PSXRD[b]	PND[c]	DFT	PSXRD[b]	PND[c]
Cu^IZn-MFU-4*l*	0.693	1.05(3)	1.003(3)	69.7	58.9(8)	60.3(1)
Cu^IMn-MFU-4*l*	0.652	0.65(2)	0.74(1)	71.0	70.5(5)	68.1(2)
Cu^ICd-MFU-4*l*	0.601	0.66(3)	n. a.	72.6	70.5(12)	n. a.
Cu^IZn-MFU-4*l*−H_2	0.940	n. a.	1.170(4)	62.6	n. a.	59.5(3)
Cu^IMn-MFU-4*l*−H_2	0.893	n. a.	1.05(1)	64.1	n. a.	59.7(3)
Cu^ICd-MFU-4*l*−H_2	0.854	0.79(1)	n. a.	65.4	66.9(4)	n. a.

[a]For DFT, the result for calculation for the corresponding $CuM_4Cl_3(bta)_6$ cluster is shown. [b]Refined by a powder synchrotron X-ray diffraction pattern collected at 153 K. [c]Refined by a powder neutron diffraction pattern collected at 7 K. Powder neutron diffraction analyses for Cu^ICd-MFU-4*l* are precluded because of the large neutron absorption cross-section of naturally abundant Cd nuclei.

dosed spectrum as a baseline for the corresponding H_2-dosed spectrum to offset the changes in framework vibrations. From our van't Hoff analyses, we find differential enthalpies of adsorption, $\Delta H°$, of −29.4(2), −23.6(2), and −17.7(2) kJ/mol and differential entropies of adsorption, $\Delta S°$, of −90.7(8), −85(1), and −68(2) J/(mol·K) for Cu^IZn-MFU-4*l*, Cu^IMn-MFU-4*l*, and Cu^ICd-MFU-4*l*, respectively (Table 2 and Figures S46, S48, and S50). Notably, the $-\Delta H°$ values are lower by 3−5 kJ/mol than $-\Delta H_{ads}$ values obtained by the aforementioned Clausius−Clapeyron analyses, as well as by density functional theory (DFT) calculations performed on a cluster model (see below). Nevertheless, our van't Hoff analyses further support that the magnitude of $\Delta H°$ follows the order Cu^IZn-MFU-4*l* > Cu^IMn-MFU-4*l* > Cu^ICd-MFU-4*l*. We also note that $-\Delta S°$ decreases as $-\Delta H°$ decreases, consistent with the positive correlation between $\Delta H°$ and $\Delta S°$.[15]

Electronic Structure Calculations. To understand the differences in electronic structure and coordination geometry of the open Cu^I sites as a function of the central metal ion, DFT calculations were performed for a cluster model of a pentanuclear secondary building unit. In this model, all $btdd^{2-}$ linkers were truncated to benzotriazolate (bta^-), a single Cu^I ion was substituted at one of the four peripheral metal sites, and chloride capping anions were placed at the other peripheral M^{II} sites, resulting in an uncharged cluster of formula $Cu_1M_4Cl_3(bta)_6$ (M = Zn, Mn, Cd; Figure 5). By normalizing the capping anion and Cu populations in each structure, we can understand how the identity of the central M^{II} ion affects H_2 binding at the peripheral Cu^I site.

https://doi.org/10.1021/jacs.4c08039
J. Am. Chem. Soc. 2024, 146, 22759−22776

The optimized geometry of the model cluster without H_2 reveals that the cluster having a larger central M ion planarizes the peripheral Cu^I site, as indicated by a longer distance between Cu atom and the plane defined by three N2 atoms (d(Cu−N2 plane)) and by a larger angle between the central M, Cu, and N2 (∠M−Cu−N2) (Table 3). Geometry optimization upon introduction of H_2 at the Cu^I site leads to Cu^I moving away from the central M^{II} ion by ∼0.25 Å for all clusters (Figure 5). This distortion is similar to what was reported in the previous study of a $Cu^I_2Zn_3$ cluster model.[41] Therefore, the trend in the extent of Cu^I pyramidalization across the Cu^IM_4 cluster models is also maintained upon H_2 binding. The H_2 molecule is predicted to be bound to the Cu^I ion in a side-on manner, with the distance between the Cu atom and the H−H centroid, d(Cu−H_2), increasing from 1.659 to 1.679 to 1.693 Å as the central ion becomes larger within the Cu^IZn_4, Cu^IMn_4, and Cu^ICd_4 clusters, respectively. The H−H distance, d(H−H), is elongated compared to that of free H_2 (0.74 Å[67]) by approximately 0.06 Å for all of the structures, suggesting partial activation of the H−H bond due to π-backbonding from Cu^I. The degree of elongation follows the trend of the size of the central ion (i.e., Cu^IZn_4 > Cu^IMn_4 > Cu^ICd_4), albeit with a subtle difference in d(H−H) across the series (0.007 Å). The differences in d(Cu−H_2) and d(H−H) calculated for the Cu^IM_4 cluster series are too subtle to probe experimentally, such as with powder neutron diffraction (PND) or inelastic neutron scattering (INS) spectroscopy. However, since DFT calculations for appropriate cluster models often reproduce H_2 binding in MOFs well,[68] the aforementioned trends in the DFT calculations are significant.

Frequency analysis with anharmonic correction predicts ν(H−H) of 3251, 3317, and 3356 cm^{-1} for the Cu^IZn_4, Cu^IMn_4, and Cu^ICd_4 clusters, respectively (Table 2). The calculated ν(H−H) frequencies agree with the experimentally observed ν(H−H) signal to within 1% difference. We note that the frequency under the harmonic approximation predicts that a value of ν(H−H) in wavenumbers is roughly 10% larger than observed, implying that the anharmonic correction is essential for accurately modeling the vibration of H_2 bound at a π-basic Cu^I site. These calculations confirm that the shift of ν(H−H) for the H_2 molecule bound to the Cu^I ion follows Cu^IZn_4 > Cu^IMn_4 > Cu^ICd_4 clusters, as observed via *in situ* gas dosing IR spectroscopy.

The calculated H_2 adsorption enthalpy, $-\Delta H^\circ_{DFT}$, is 31.6, 26.7, and 24.0 kJ/mol for the Cu^IZn_4, Cu^IMn_4, and Cu^ICd_4 clusters, respectively (Table 2). These values are close to the isosteric enthalpy of H_2 adsorption, $-\Delta H_{ads}$, obtained from the Clausius−Clapeyron analysis discussed above. While the computational results are obtained for a $Cu_1M_4Cl_3(bta)_6$ cluster with only one Cu^I per cluster, computation for clusters with either two or three Cu^I sites yield similar results in coordination structures around Cu^I−H_2 and the thermodynamics for H_2 binding (Tables S6 and S7). The second and third H_2 molecules to bind at a cluster are calculated to be slightly weaker than the first binding event by 1−2 kJ/mol, which is minor and can be considered negligible, especially when compared to the differences in the calculated adsorption enthalpies among the Cu^IM_4 clusters. This illustrates the significance of the identity of the central metal of the secondary building unit in controlling H_2 binding at peripheral Cu^I sites. Additionally, H_2 binding for the Cu^I sites in the same cluster have minimal cooperativity between Cu^I sites. Indeed, the plot of ΔH_{ads} against H_2 loading in Figure 3d suggests H_2 adsorption in Cu^IM-MFU-4*l* frameworks reveals almost constant ΔH_{ads} until saturation of the Cu^I sites. The experimental ΔH_{ads} plot can be interpreted as an averaged value for clusters with different numbers of Cu^I sites and clusters with different H_2 loading.

We employed an energy decomposition analysis based on absolutely localized molecular orbitals (ALMO-EDA) to understand the nature of the binding interaction between Cu^I and H_2 (Table 4).[69−71] The largest difference in interaction components among the Cu^IM-MFU-4*l* cluster models is found in the charge transfer term (ΔE_{CT}) while the other terms are almost constant upon alteration of the identity of M. Specifically, the magnitude of ΔE_{CT} follows the trend of Cu^IZn_4 > Cu^IMn_4 > Cu^ICd_4 clusters. Further, the charge transfer from Cu^I to H_2 is the largest for the Cu^IZn_4 cluster and the smallest for the Cu^ICd_4 cluster. Overall, the DFT calculations support our hypothesis that having a larger metal ion at the center of a pentanuclear cluster leads to an open Cu^I site with a more planar geometry that consequently shows weaker π-backbonding.

Table 4. Energy Decomposition Analysis of Binding Energies and Charge Transfer to the H_2 Molecule Obtained with ALMO-EDA Method

contribution	Cu^IZn_4	Cu^IMn_4	Cu^ICd_4
		energy (kJ/mol)	
ΔE_{prep}[a]	15.7	15.9	15.7
ΔE_{frz}[b]	41.4	42.4	43.2
ΔE_{pol}[c]	38.5	37.2	36.7
ΔE_{CT}[d]	51.3	48.4	46.8
ΔE_{total}	32.6	27.3	24.6
		charge transfer (e)	
$Cu^I \rightarrow H_2$	0.0501	0.0475	0.0464

[a]Energy required to distort each fragment to the geometry in the bonded state. [b]Energy change arising without relaxation of the fragment orbitals, which includes interfragment electrostatics, Pauli repulsion, and dispersion interaction. [c]Energy arising from relaxation of self-contained fragment orbitals in the presence of the field of the other fragment. [d]Stabilization energy by charge transfer between the fragments.

Powder Neutron Diffraction. Previously, an *in situ* D_2-dosing powder neutron diffraction analysis for Cu^IZn-MFU-4*l* suggested the presence of a metastable physisorption precursor for hydrogen adsorption.[41] Briefly, a change in the cubic unit cell parameter upon D_2 dosing depended on the D_2 dosing temperature. Dosing D_2 at 40 K led to a contraction of the unit cell parameter by 0.057(2) Å while dosing the same amount of D_2 at 300 K led to a contraction of the unit cell parameter by 0.124(2) Å, with both of the diffraction patterns collected at 7 K. Rietveld refinements further revealed a greater occupancy of D_2 at the Cu^I site for D_2 dosing at higher temperatures. This observation indicates the presence of an activation barrier in Cu^I pyramidalization upon D_2 adsorption, accompanied by a unit cell contraction. Gas dosing at 40 K does not readily allow the Cu^I sites to undergo pyramidalization to enable π-backbonding-mediated strong adsorption, therefore resulting in only a very slight unit cell contraction. Here, we are interested in whether Cu^IMn-MFU-4*l* and Cu^ICd-MFU-4*l*, which exhibit weaker π-backbonding, also show similar behavior upon hydrogen adsorption. Unfortunately, the large neutron absorption cross-section of naturally abundant

https://doi.org/10.1021/jacs.4c08039
J. Am. Chem. Soc. 2024, 146, 22759−22776

Table 5. Cubic Unit Cell Parameter a and D_2 Occupancies Determined by Powder Neutron Diffraction[a]

condition	description	a (Å)	d(Cu−D_2[site I]) (Å)	D_2 occupancies per Cu[b]	
				site I	site II
activated	under vacuum	31.6357(8)	n.a.	n.a.	n.a.
1	dosing 0.75 equiv D_2 at 40 K	31.5687(14)	1.65(4)	0.41(2)	0.36(2)
2	dosing 0.75 equiv D_2 at 40 K, followed by warming and cooling	31.4270(9)	1.54(2)	0.75(1)	0

[a]All diffraction patterns were collected at 7 K. [b]The reported occupancies here are the occupancies as a D_2 molecule divided by the occupancy of Cu (0.675, corresponding to 2.7 Cu per cluster as estimated by ICP-OES).

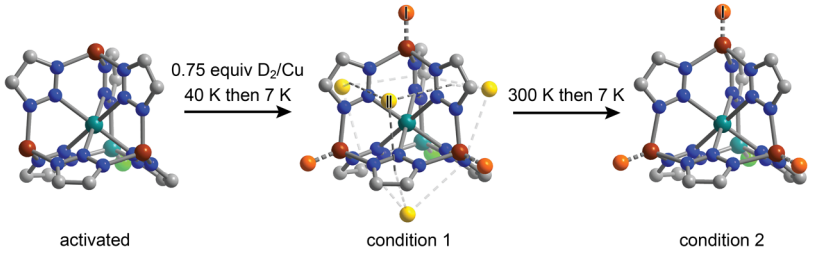

Figure 6. Schematic illustration of D_2 adsorption sites in Cu^IMn-MFU-4*l* refined against powder neutron diffraction patterns collected at 7 K for various cooling and heating cycles. Brown, blue, gray, emerald green, and light green spheres represent Cu, N, C, Mn, and Cl atoms, respectively, whereas orange and yellow spheres represent centroids of D_2 for site I and site II, respectively, as refined with the super atom approach.

isotopes of Cd precludes neutron diffraction analysis for Cu^ICd-MFU-4*l*.[72] We therefore decided to focus on a powder neutron diffraction analysis of Cu^IMn-MFU-4*l*.

Diffraction patterns were collected under various temperatures and gas atmosphere conditions and Rietveld refinements were conducted to examine the structures of activated and D_2-dosed Cu^IMn-MFU-4*l* under various conditions. Full refinement procedures are presented in the SI, while selected structural parameters are summarized in Tables 3 and 5. We employed the super atom approach to model the scattering from the D_2 molecule, in which a single super atom represents the centroid of the D_2 molecule possessing anomalously large displacement parameters due to the quantum rotational excitation. Thus, a single super atom can have an occupancy of up to two D atoms to represent one D_2 molecule (the occupancies presented below are converted to the occupancies as a D_2 molecule for simplicity).[73]

A refinement of the structure against the powder neutron diffraction pattern collected at 7 K for Cu^IMn-MFU-4*l* dosed with 0.75 equiv of D_2 at 40 K (condition 1) yielded a unit cell parameter contracted by only 0.067(2) Å compared to the activated framework, and revealed two D_2 adsorption sites. Site I occurs adjacent to the Cu^I sites, with d(Cu−D_2) = 1.65(4) Å and an occupancy of 0.28(2) (i.e., 0.41(2) D_2 per Cu). We find a slight increase in pyramidalization of the Cu centers (d(Cu−N2 plane): 0.74(1) Å for the activated framework and 0.87(2) Å for condition 1). Site II occurs in the "bowl" site with framework−gas interactions formed between the triazole rings and the D_2 molecule. The distance from the centroid of the triazole moiety to the gas molecule d(triazole···D_2) is 3.60(3) Å, indicating modest van der Waals interactions with the framework. The occupancy at site II is 0.25(2) (i.e., 0.36(2) D_2 per Cu). The total refined occupancy of gas molecules sums to 0.78(4) D_2 per Cu center in agreement with the amount of gas added to the system, indicating complete adsorption of the dosed D_2.

A refinement of the structure against the powder neutron diffraction pattern collected after dosing 0.75 equiv of D_2 followed by warming to 300 K and cooling to 7 K (condition 2) shows a unit cell parameter that is contracted by 0.142(2) Å compared to that for condition 1. The occupancy at site I approaches 0.75 equiv of D_2 per Cu while the occupancy at site II refines to zero within error. The new framework−gas distance refines to d(Cu−D_2) = 1.54(2) Å, which is ∼0.1 Å shorter compared to that obtained for condition 1 and is within error of the value found for D_2 strongly bound to Cu^I in Cu^IZn-MFU-4*l*, d(Cu−D_2) = 1.53(2) Å (Figure 6).[41] The refined structure also reveals an increase in Cu^I pyramidalization, as evident in the elongated distance to the plane of the three coordinating N atoms: d(Cu−N2 plane) = 1.05(1) Å for condition 2 vs d(Cu−N2 plane) = 0.87(2) Å for condition 1. Overall, the sharp decrease in unit cell parameter and the increase in the D_2 occupancy of site I by warming and subsequent cooling suggests that the strong adsorption site at Cu^I is not readily available for D_2 at 40 K, thus implying the presence of an activation barrier for strong D_2 adsorption at the Cu^I sites, as previously observed for Cu^IZn-MFU-4*l*.[41]

Powder Synchrotron X-ray Diffraction. Since we were not able to obtain *in situ* D_2-dosing powder neutron diffraction data for Cu^ICd-MFU-4*l*, we investigated whether a structural change is observed upon H_2 dosing for Cu^ICd-MFU-4*l* by *in situ* H_2-dosing powder X-ray diffraction with synchrotron radiation. The sample was activated under dynamic vacuum at 373 K prior to collecting diffraction patterns at 153 K on the activated framework. Subsequently, H_2 was dosed to approximately 140 mbar at equilibration to ensure the saturation of Cu^I sites with H_2. The Rietveld refinements against the diffraction patterns of the activated and H_2-dosed Cu^ICd-MFU-4*l* show a decrease in the unit cell parameter by 0.095(1) Å from 31.677(1) to 31.5825(7) Å. This magnitude of contraction is similar to the powder neutron diffraction results for Cu^IMn-MFU-4*l* and Cu^IZn-MFU-4*l*. The d(Cu−N2 plane) is revealed to increase from 0.66(3) Å to 0.79(1) Å (Table 3), consistent with the increased pyramidalization upon H_2 adsorption. In view of the negligible cross-section of H atoms and the assumed proximity of the H_2 molecules to heavy Cd and I atoms in the model, H_2 molecules were not included in the refinement.

The compounds Cu^IZn-MFU-4*l* and Cu^IMn-MFU-4*l* were also analyzed with powder synchrotron X-ray diffraction at the

https://doi.org/10.1021/jacs.4c08039
J. Am. Chem. Soc. 2024, 146, 22759−22776

same condition for comparison with $Cu^{I}Cd$-MFU-4*l* (Table 3). Overall, Rietveld refinements agree that the Cu sites become closer to planar as the central ion of the cluster becomes larger, although *d*(Cu−N2 plane) and ∠M−Cu−N2 refined from the diffraction experiments do not agree well with those obtained from DFT calculations performed on a cluster model. These discrepancies likely arise from the difference between the extended lattice structure of a framework versus the molecular cluster model employed in the DFT calculation. It should also be noted that the partial occupancy of Cu that is almost overlapping with the peripheral M^{II} ion generally makes it difficult to analyze the coordination geometry of Cu sites crystallographically. Nevertheless, the observed unit cell contraction upon H_2 dosing implies that the change in the coordination geometry of Cu upon H_2 adsorption generally occurs in all $Cu^{I}M$-MFU-4*l* frameworks, as predicted by the DFT calculations, even when the H_2 binding becomes weaker in $Cu^{I}Mn$- and $Cu^{I}Cd$-MFU-4*l*.

Inelastic Neutron Scattering Spectroscopy. Inelastic neutron scattering (INS) experiments were undertaken to further understand the $Cu^{I}-H_2$ interaction in $Cu^{I}Mn$-MFU-4*l*. Specifically, INS can examine rotational transitions of an H_2 molecule bound to a metal, and thus has been used to probe the barrier of rotation of an H_2 molecule bound to a metal[74] or the elongation of the H−H bond due to π-backbonding using the rotational constant *B*.[66] We note that INS measurements for $Cu^{I}Cd$-MFU-4*l* are also hindered by the large neutron absorption cross-section of naturally abundant isotopes of Cd. The background subtracted INS spectrum for $Cu^{I}Mn$-MFU-4*l* dosed with 0.75 equiv of *para*-H_2 are plotted in Figure 7. The

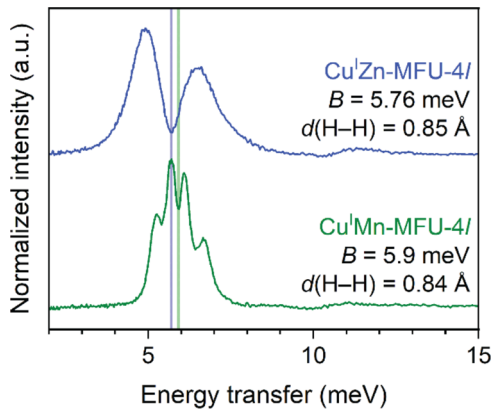

Figure 7. INS spectra for $Cu^{I}Mn$-MFU-4*l* (green) and $Cu^{I}Zn$-MFU-4*l*[66] (blue) dosed with *para*-H_2 from 2 to 15 meV. A spectrum shown here is difference between the spectrum of an activated framework and that after *para*-H_2 dosing.

spectrum shows four peaks in the low energy transfer region, occurring at energy transfer values of 5.278(6), 5.714(3), 6.098(3), and 6.642(8) meV. Given the relative intensities, we tentatively attribute these peaks as two sets of splitting peaks with $J = 0$ to $J = 1$ rotational excitations for *para*-H_2 in slightly different rotational potential environments. Additional features are observed between 30 and 45 meV (Figure S74), which can be assigned as combination bands and overtones from H_2 on the same binding sites as the low energy transfer peaks, as observed in similar studies.[75,76]

Next, we turned to a simple analytical model for a quasi-two-dimensional (quasi-2D) rotor, which has been used to estimate excitation energies for INS spectra of H_2-dosed materials in the past, including for H_2-dosed $Cu^{I}Zn$-MFU-4*l*.[66] This model only assumes a simplified (effective) shape for the three-dimensional potential landscape around H_2.[27,76] We attempted to analyze our data using this model solely for the purpose of comparing the INS results for $Cu^{I}Mn$-MFU-4*l* with the previous analysis for $Cu^{I}Zn$-MFU-4*l*.[66] In a quasi-2D rotor model, the potential energy can be described by the following equation,[77]

$$V(\theta, \phi) = \left(a + \frac{b}{2}\cos 2\phi\right)\sin^2\theta$$

where θ is the angle between the H−H bond and the *z*-axis connecting the center of the molecule and the Cu atom (polar angle), ϕ is the angle within the plane perpendicular to the *z*-axis (azimuthal angle), and *a* and *b* are parameters describing the strength and anisotropy of the potential.

The above potential profile of a quasi-2D rotor, for which the Schrödinger equation can be solved numerically (Figure S73), can explain the observation of four peaks in the low energy transfer region for H_2-dosed $Cu^{I}Mn$-MFU-4*l*. For a quasi-2D rotor with strong interactions (very negative *a*), the lowest excitation energy (J_0M_0 to $J_1M_{\pm1}$, which is doubly degenerate when *b* is zero) should have an energy converging to the rotational constant *B*, which is inversely proportional to the bond length squared for a diatomic molecule in the rigid motor model. When *b* is greater than zero, which means the potential energy in the 2D plane is anisotropic, the doubly degenerated energy level should split with the gap increasing with *b*. Therefore, we interpret the four peaks in the low energy transfer region of the spectrum as two sets of splitting peaks centering around 5.9 meV with different *b* values. This peak center would yield a rotational constant $B = 5.9$ meV, which is smaller than that of free H_2 ($B = 7.54$ meV[67]) in a 2D-rotor model with very negative *a* ($a \rightarrow -\infty$), therefore suggesting an elongated H−H distance of 0.84 Å. Based on the Cu:Mn ratio determined by ICP-OES (Cu:Mn = 2.7:2.3), we assume that the set of peaks with smaller splitting (thus smaller *b* or in-plane anisotropy) with higher intensity are associated with Cu_3Mn_2 clusters (assumed 70% prevalence), whereas the set with larger splitting (thus larger *b* or in-plane anisotropy) with lower intensity are associated with Cu_2Mn_3 clusters (assumed 30% prevalence). This suggests that the number of unsaturated Cu^{I} sites present locally per cluster affects the dynamics of that cluster upon H_2 adsorption, which in turn effects the enthalpy of adsorption, as observed in DFT calculation for cluster models with different number of Cu^{I} sites. This may also partly contribute to the broadened peaks observed in the infrared spectra.

We also compared the presented INS results with those reported for $Cu^{I}Zn$-MFU-4*l* previously (Figure 7, blue line).[66] In contrast to the spectrum of $Cu^{I}Mn$-MFU-4*l* showing four peaks in the low energy transfer region, there are only two somewhat broader peaks in the spectrum for $Cu^{I}Zn$-MFU-4*l*, suggesting that the local clusters have a more uniform composition (likely Cu_2Zn_3 clusters). The splitting of the peaks (4.97 and 6.54 meV) is larger than that observed in $Cu^{I}Mn$-MFU-4*l*, and the center at 5.76 meV is slightly lower, corresponding to a slightly longer calculated H−H bond of 0.85 Å. These observations suggest that the Cu−H_2 interaction in $Cu^{I}Zn$-MFU-4*l* is stronger and more anisotropic than in $Cu^{I}Mn$-MFU-4*l*, consistent with H_2 adsorption isotherms and analyses of *in situ* H_2-dosed infrared spectra.

https://doi.org/10.1021/jacs.4c08039
J. Am. Chem. Soc. 2024, 146, 22759−22776

High-Pressure H_2 Adsorption Properties. In the previous sections, we reported that the size of the central metal ion of the pentanuclear cluster of Cu^IM-MFU-4*l* affects the H_2 adsorption below 1 bar arising from H_2−Cu^I coordination. For realistic demonstration of H_2 storage with Cu^IM-MFU-4*l* frameworks, it is critical to assess how differences in H_2 binding energy at primary adsorption sites affect H_2 adsorption profiles under practical operation conditions of H_2 storage (i.e., at near-ambient temperatures and higher pressures). Therefore, we measured high-pressure H_2 adsorption isotherms at pressures as high as 190 bar from 223 to 323 K (Figures 8 and S75−S78). As a reference, we also collected the isotherms for ZnCl-MFU-4*l*, for which H_2 uptake originates only from weak physisorption at non-Cu adsorption sites. For facile comparison, the obtained excess gravimetric H_2 uptake data were converted to the excess volumetric uptake by employing the crystallographic density of each activated framework (Table S11).

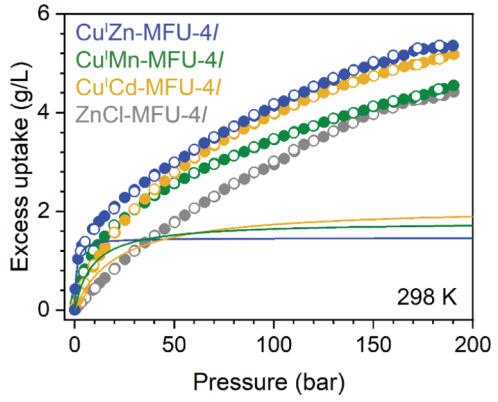

Figure 8. High-pressure H_2 adsorption isotherms obtained for ZnCl-MFU-4*l* (gray) and Cu^IM-MFU-4*l* with M = Zn (blue), Mn (green), and Cd (yellow) at 298 K up to 190 bar. Filled and open circles represent adsorption and desorption branches, respectively. Solid lines represent a simulated H_2 uptake for stronger adsorption sites at exposed Cu^I sites obtained by a dual-site Langmuir model.

All MFU-4*l* frameworks exhibit a gradual increase in H_2 uptake upon dosing H_2 up to 190 bar, with no hysteresis upon desorption at the examined temperatures (Figures S75−S78). Expectedly, the curvature of an adsorption isotherm depends on the chemical composition of the pentanuclear cluster of the framework. The compound ZnCl-MFU-4*l* exhibits the least curvature and a nearly linear profile in its H_2 adsorption isotherms up to 190 bar without plateauing. Such a profile is characteristic of highly porous frameworks without strong H_2 adsorption sites. In contrast, the isotherms for Cu^IM-MFU-4*l* frameworks are more curved due to the strong H_2 binding to the Cu^I sites. Among them, Cu^IZn-MFU-4*l* reveals the steepest initial H_2 uptake. Interestingly, the adsorption profile for Cu^IZn-MFU-4*l* above 5 bar at a given temperature appears almost parallel to the corresponding isotherm of ZnCl-MFU-4*l*. This observation prompted us to deconvolute the H_2 uptake in Cu^IZn-MFU-4*l* into strong H_2 binding at Cu^I sites and weak physisorption at non-Cu^I adsorption sites by fitting the adsorption isotherm data with a dual-site Langmuir equation. Gratifyingly, the H_2 uptake can be modeled well by this approach, with the resulting fit parameters indicating the presence of a small number of strong adsorption sites and a larger number of weak adsorption sites. We generated two sets of simulated isotherms with these fitting parameters for strong and weak adsorption sites, assuming that these adsorption sites behave independently within the same material (Figure S79). The profile of the simulated adsorption isotherm for the weak adsorption sites in Cu^IZn-MFU-4*l* resembles the H_2 isotherm profile for ZnCl-MFU-4*l* within 10% difference, while the slight difference can arise from the difference in the pore size. Notably, the calculated saturation capacity for the strong adsorption sites (1.4 mmol/g) is consistent with the number of active Cu^I sites, as estimated from the steep H_2 uptake at 77 K (Figure 3a). Therefore, it is reasonable to conclude that the deconvoluted H_2 adsorption profile allows evaluation of how the coverage of Cu^I sites changes by increasing H_2 pressure.

The high-pressure H_2 adsorption isotherms of Cu^IMn-MFU-4*l* and Cu^ICd-MFU-4*l* were also fitted using a dual-site Langmuir equation to extract the H_2 adsorption behavior of the Cu^I site (Table S12). As shown as solid lines in Figure 8, simulated H_2 isotherms for the stronger adsorption sites (i.e., Cu^I sites) for these Cu^IM-MFU-4*l* frameworks at 298 K exhibit steep initial H_2 uptake followed by a plateau region. However, Cu^IMn-MFU-4*l* and Cu^ICd-MFU-4*l* showed more gently curved simulated isotherms at low pressure and higher saturation pressure than Cu^IZn-MFU-4*l*. The estimated surface coverage for the Cu^I sites at 5 bar and 298 K is 85, 36, and 19% for Cu^IZn-MFU-4*l*, Cu^IMn-MFU-4*l*, and Cu^ICd-MFU-4*l*, respectively, while at 100 bar it is 99, 92, and 83%, respectively. Thus, the fraction of the usable Cu^I sites for a 5−100 bar

Table 6. Summary of the Usable Capacities in g/L and wt % for Selected Conditions, Weighted Average of Adsorption Enthalpies, $\Delta H^\circ_{w.ave}$, and Heterogeneity Parameters, *s*

	total usable capacities						
	298 K, 100 bar → 298 K, 5 bar		223 K, 170 bar → 298 K, 5 bar		$\Delta H^\circ_{w.ave}$ [a]	*s* [b]	
materials	g/L	wt %	g/L	wt %	−kJ/mol	−kJ/mol	reference
ZnCl-MFU-4*l*	8.5	1.5	19.7	3.4	4.1	n.a.	this work
Cu^IZn-MFU-4*l*	8.2	1.6	18.8	3.5	4.9	15.3	this work
Cu^IMn-MFU-4*l*	6.8	1.4	13.8	2.8	4.0	12.2	this work
Cu^ICd-MFU-4*l*	8.5	1.4	18.3	3.1	4.6	8.6	this work
Ni_2(*m*-dobdc)	11	0.91	no data		6.7	3.9	32
$V_2Cl_{2.8}$(btdd)	9.6	1.5	no data		4.8	12.7	35
NU-2100	6.7	0.40	no data		5.5	14.2	44

[a]Calculated based on the saturation capacity and the enthalpy term obtained by fit to a dual-site Langmuir model. [b]$s = (\Delta H^\circ_{max} - \Delta H^\circ_{min})/2$, where ΔH°_{max} and ΔH°_{min} are the maximum and minimum values of in the enthalpy term, respectively, obtained by fit to a dual-site Langmuir model.

https://doi.org/10.1021/jacs.4c08039
J. Am. Chem. Soc. 2024, 146, 22759−22776

pressure swing is estimated to be 14, 56, and 63% for Cu^{I}Zn-MFU-4*l*, Cu^{I}Mn-MFU-4*l*, and Cu^{I}Cd-MFU-4*l*, respectively. A similar calculation for a 5−170 bar swing at 298 K yields 14, 59, and 70%, respectively. Note that the usable fraction of the Cu^{I} sites in Cu^{I}Cd-MFU-4*l* matches the theoretical maximum value for the usable fraction for the condition of interest (63 and 70% for 5−100 and 5−170 bar swings, respectively). These analyses suggest that the H_2 binding strength at Cu^{I} sites in Cu^{I}Cd-MFU-4*l* is indeed optimal for maximizing the usable fraction of the adsorption sites for ambient-temperature storage.

To evaluate the total usable capacity of H_2 for the materials under practical operational conditions, we calculated the total H_2 uptake,[78,79] which can be defined as the sum of the adsorbed H_2 and the amount of free H_2 in the pore—i.e., the product of pore volume and bulk H_2 density at the storage condition (Figures S75−S78). The usable capacity is obtained by subtracting the total uptake at the discharge condition from that at the charging condition (Table 6). Significantly, the volumetric usable capacities for Cu^{I}M-MFU-4*l* are comparable to or slightly lower than that for ZnCl-MFU-4*l*. We reason that the amount of H_2 that is weakly physisorbed and located within the void space of the frameworks is 4−6 times greater than the H_2 uptake originating from the Cu^{I} sites in a Cu^{I}M-MFU-4*l* framework because the number of the Cu^{I} sites is much lower than that of weak adsorption sites even though the fraction of the usable weak adsorption sites may not be high. Furthermore, the porosity of the Cu^{I}M-MFU-4*l* frameworks was compromised after the Cu^{I}-exchange (Table 1), which decreased the contribution from the free H_2 in the pore. The framework Cu^{I}Cd-MFU-4*l* could outperform ZnCl-MFU-4*l* by 10% in volumetric usable H_2 capacity for a 2−35 bar pressure swing at 298 K. At these conditions, the combined contribution from weak physisorption and free H_2 in the pore is small relative to that from adsorption at the Cu^{I} sites. Notably, operation at such lower pressures (20−48 bar) is relevant to the last-mile distribution of hydrogen[80] and the charging at 35 bar is achievable by single-stage compressors.[81]

The Cu^{I}M-MFU-4*l* materials clearly have more than one type of adsorption site, in view of crystallographic and spectroscopic data, as the high-pressure H_2 adsorption isotherm data. Indeed, the effect of thermodynamic parameters on the usable capacity of an adsorbent has mainly been considered for an energetically homogeneous adsorbent (i.e., a single-site Langmuir model). However, actual adsorbents usually contain weak H_2 binding sites and pore space for free H_2, even if strong H_2 binding sites are also present. Although it is difficult to describe the adsorption properties of heterogeneous materials because the usable capacity varies with the degree of heterogeneity, a weighted average of adsorption enthalpy of multiple binding sites ($\Delta H^{\circ}_{w.ave}$) and a heterogeneity parameter, $s = (\Delta H^{\circ}_{max} - \Delta H^{\circ}_{min})/2$, where ΔH°_{max} and ΔH°_{min} are the maximum and minimum values of adsorption enthalpy, respectively, can be a good measure.[17] Ideal adsorbent materials are expected to have the weighted average of adsorption enthalpy within the optimal range (i.e., from −15 to −25 kJ/mol) and a small heterogeneity parameter so that extreme adsorption and desorption conditions are not required.

To assess their utility in establishing hydrogen storage performance, the weighted average of adsorption enthalpy and the heterogeneity parameter for the MFU-4*l* frameworks and selected framework materials were estimated with fit parameters for the total high-pressure H_2 isotherms in a dual-site Langmuir model (Tables 6, S13, and S14). The weighted average of adsorption enthalpies for MFU-4*l* frameworks is −4 to −5 kJ/mol in all cases, indicating that the weak adsorption sites dominate the total uptake of H_2 in the MFU-4*l* frameworks. In contrast, Ni_2(*m*-dobdc)—the current benchmark adsorbent for ambient-temperature H_2 storage—shows a higher weighted average of adsorption enthalpy and a smaller heterogeneity parameter than Cu^{I}M-MFU-4*l*-type materials and other frameworks with strong H_2 binding sites. This finding indicates that a high density of open Ni^{II} sites is critical for enhancing the weighted average of adsorption enthalpies in Ni_2(*m*-dobdc) (despite a reported isosteric enthalpy of adsorption that is slightly lower than optimal: −12.3 kJ/mol), while also contributing a higher volumetric usable capacity than is observed in the MFU-4*l* frameworks presented here. For improving the total usable H_2 storage capacity, a higher density of the adsorption sites with a binding enthalpy in the optimal range of −15 to −25 kJ/mol is clearly a requirement. Considering that Ni_2(*m*-dobdc) exhibits one of the highest open metal site densities among framework materials, incorporation of strong H_2 binding sites capable of binding multiple H_2 per metal site could be an upcoming strategy to drastically increase the H_2 storage capacity in addition to selecting the suitable framework porosity and topology that maximize the density of the open metal sites.[4,68,82]

CONCLUSIONS AND OUTLOOK

The foregoing results show that the π-basicity of the Cu^{I} sites in the Cu^{I}M-MFU-4*l* (M = Zn, Mn, and Cd) series of metal−organic frameworks can be deliberately controlled by changing the radius of the central metal ion in the pentanuclear cluster node. Compared with Lewis acidic open metal sites in typical MOFs, π-basic open metal sites enable a higher magnitude of adsorption enthalpy than Lewis acidic metal sites for π-acidic gases. Consequently, the Cu^{I}M-MFU-4*l* frameworks serve as rare examples of materials exhibiting a high isosteric enthalpy of H_2 adsorption (−33.4, −26.9, and −22.7 kJ/mol for M = Zn, Mn, and Cd, respectively). Among the series, Cu^{I}Cd-MFU-4*l* is only the second example of a MOF displaying an H_2 binding enthalpy within the optimal range for ambient-temperature hydrogen storage. Additionally, the magnitude of the change in the adsorption enthalpy in the Cu^{I}M-MFU-4*l* series is significantly larger than observed in several isostructural frameworks containing different metals or anions (Figure 9). Note that the difference in enthalpy of the Cu^{I}M-MFU-4*l* series arises from tuning the central metal ion of the pentanuclear cluster nodes—a metal center that is located three bonds away from the open Cu^{I} sites that directly engage with H_2. The series thus presents an unprecedented system for varying the isosteric enthalpy of H_2 adsorption and therefore the hydrogen storage capacity of a material. This situation is in sharp contrast to the H_2 adsorption at Lewis acidic metal sites in MOFs, which is less tunable even by changing the identity of open metal sites.

This study demonstrates a means of controlling the orbital-interaction-mediated H_2 adsorption within MFU-4*l*-type frameworks featuring pentanuclear triazolate-bridged cluster nodes. We anticipate that this concept can be directly applied to other frameworks materials known to have the same cluster nodes.[47,48,84] More broadly, because a myriad of such nodes are known to exist in extended framework structures,[85] a

https://doi.org/10.1021/jacs.4c08039
J. Am. Chem. Soc. 2024, 146, 22759−22776

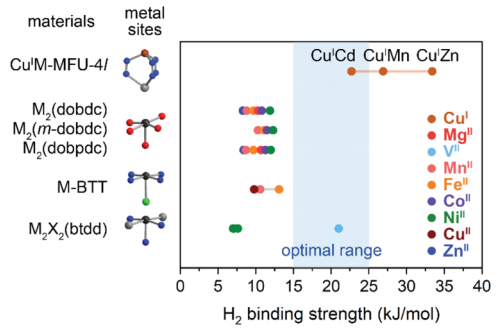

Figure 9. Summary of isosteric enthalpy of H_2 adsorption ($-\Delta H_{ads}$) by the Clausius−Clapeyron method in selected MOFs featuring open metal sites: M_2(dobdc) (dobdc^{4-} = 2,5-dioxido-1,4-benzenedicarboxylate),[19,27,83] M_2(*m*-dobdc) (*m*-dobdc^{4-} = 4,6-dioxido-1,3-benzenedicarboxylate),[27] M_2(dobpdc) (dobpdc^{4-} = 4,4′-dioxidobiphenyl-3,3′-dicarboxylate),[29] M-BTT ($M_3[(M_4Cl)_3(BTT)_8]_2$: BTT^{3-} = 1,3,5-benzenetristetrazolate),[26] and M_2X_2(btdd).[30,35] The color of each circle symbol in the figure specifies the identity of the metal ion of an open metal site, as shown at the bottom right. The coordination environment of the open metal site of each class of MOFs is shown at the right of the name of the corresponding framework. Brown, blue, red, and light green spheres represent Cu, N, O, and Cl atoms, respectively. The black spheres represent an unspecified metal atom, whereas the gray spheres represent unspecified atoms that can be varied to tune the adsorption properties of open metal sites.

similar concept could potentially translate to other framework materials with secondary building units featuring an interstitial metal site. We therefore anticipate that the careful design of geometries and electronic structures of open metal sites may enable us to create MOFs that modulate the orbital-interaction-mediated H_2 adsorption, giving rise to new materials that range from exhibiting an optimal binding strength for ambient temperature storage to facilitating dissociative H_2 chemisorption and the realization of porous metal hydrides.

While this study and previous studies have focused on how the hydrogen storage properties of a porous material can be estimated from its H_2 adsorption isotherms, the assessment of such materials should also account for their performance under more realistic storage conditions. For instance, hydrogen fuel produced by water splitting likely contains O_2 and H_2O at ppm concentrations.[86] Testing the charging cyclability of Cu^{I}M-MFU-4l and traditional MOFs featuring Lewis acidic metal sites with fuel-grade hydrogen gas under practical fuel cell operation conditions will be of interest for the development of practically relevant hydrogen storage materials. Notably, Cu^{I}Zn-MFU-4l has recently been examined for the separation of oxygen from air, demonstrating fully reversible O_2 binding even the presence of water vapor.[58] We expect that the low affinity of Cu^{I}M-MFU-4l for potential impurities in hydrogen fuels will be advantageous for their use in storage applications, considering that classical Lewis acidic metal sites are typically hygroscopic, which could potentially deactivate metal sites in the presence of water. Relatedly, we note that $V_2Cl_{2.8}$(btdd), the only other MOF known to exhibit H_2 binding in the optimal range, is irreversibly oxidized by air, permanently degrading the V^{II} sites in the presence of O_2.[34,35] Clearly, it is worthwhile to pursue analogues of the Cu^{I}M-MFU-4l materials that possess a higher density of Cu^{I} sites per unit volume, thereby enhancing the volumetric H_2 storage capacity. Efforts to synthesize such materials are ongoing.

■ ASSOCIATED CONTENT

Supporting Information

The Supporting Information is available free of charge at https://pubs.acs.org/doi/10.1021/jacs.4c08039.

Detailed experimental procedures, synthetic procedures, full characterizations of the reported compounds, full gas adsorption data, additional spectroscopic data, X-ray crystallographic information, full neutron diffraction data, and computational information (PDF)

Adsorption information files (ZIP)

Cartesian coordinates of the optimized geometries of the computational cluster models (XYZ)

Accession Codes

CCDC 2352603−2352604 and 2352998−2353005 contain the supplementary crystallographic data for this paper. These data can be obtained free of charge via www.ccdc.cam.ac.uk/data_request/cif, or by emailing data_request@ccdc.cam.ac.uk, or by contacting The Cambridge Crystallographic Data Centre, 12 Union Road, Cambridge CB2 1EZ, UK; fax: + 44 1223 336033.

■ AUTHOR INFORMATION

Corresponding Author

Jeffrey R. Long − *Department of Chemistry, University of California, Berkeley, California 94720, United States; Department of Chemical and Biomolecular Engineering, Department of Materials Science and Engineering, and Institute for Decarbonization Materials, University of California, Berkeley, California 94720, United States; Materials Sciences Division, Lawrence Berkeley National Laboratory, Berkeley, California 94720, United States;* orcid.org/0000-0002-5324-1321; Email: jrlong@berkeley.edu

Authors

Yuto Yabuuchi − *Department of Chemistry, University of California, Berkeley, California 94720, United States; Institute for Decarbonization Materials, University of California, Berkeley, California 94720, United States; Materials Sciences Division, Lawrence Berkeley National Laboratory, Berkeley, California 94720, United States;* orcid.org/0000-0003-3034-558X

Hiroyasu Furukawa − *Department of Chemistry, University of California, Berkeley, California 94720, United States; Institute for Decarbonization Materials, University of California, Berkeley, California 94720, United States; Materials Sciences Division, Lawrence Berkeley National Laboratory, Berkeley, California 94720, United States;* orcid.org/0000-0002-6082-1738

Kurtis M. Carsch − *Department of Chemistry, University of California, Berkeley, California 94720, United States; Institute for Decarbonization Materials, University of California, Berkeley, California 94720, United States;* orcid.org/0000-0003-4432-7518

Ryan A. Klein − *Material, Chemical, and Computational Sciences Directorate, National Renewable Energy Laboratory, Golden, Colorado 80401, United States; Center for Neutron Research, National Institute of Standards and Technology, Gaithersburg, Maryland 20899, United States;* orcid.org/0000-0002-6807-6701

Nikolay V. Tkachenko − *Department of Chemistry, University of California, Berkeley, California 94720, United States;*

Institute for Decarbonization Materials, University of California, Berkeley, California 94720, United States; Materials Sciences Division, Lawrence Berkeley National Laboratory, Berkeley, California 94720, United States; orcid.org/0000-0002-7296-4293

Adrian J. Huang − *Department of Chemistry, University of California, Berkeley, California 94720, United States; Institute for Decarbonization Materials, University of California, Berkeley, California 94720, United States; Materials Sciences Division, Lawrence Berkeley National Laboratory, Berkeley, California 94720, United States*

Yongqiang Cheng − *Neutron Scattering Division, Oak Ridge National Laboratory, Oak Ridge, Tennessee 37831, United States;* orcid.org/0000-0002-3263-4812

Keith M. Taddei − *Neutron Scattering Division, Oak Ridge National Laboratory, Oak Ridge, Tennessee 37831, United States*

Eric Novak − *Neutron Scattering Division, Oak Ridge National Laboratory, Oak Ridge, Tennessee 37831, United States;* orcid.org/0000-0001-7813-1180

Craig M. Brown − *Center for Neutron Research, National Institute of Standards and Technology, Gaithersburg, Maryland 20899, United States; Department of Chemical and Biomolecular Engineering, University of Delaware, Newark, Delaware 19716, United States;* orcid.org/0000-0002-9637-9355

Martin Head-Gordon − *Department of Chemistry, University of California, Berkeley, California 94720, United States; Institute for Decarbonization Materials, University of California, Berkeley, California 94720, United States; Chemical Sciences Division, Lawrence Berkeley National Laboratory, Berkeley, California 94720, United States;* orcid.org/0000-0002-4309-6669

Complete contact information is available at: https://pubs.acs.org/10.1021/jacs.4c08039

Notes

The authors declare no competing financial interest.

■ ACKNOWLEDGMENTS

This research was supported by the Hydrogen Materials—Advanced Research Consortium (HyMARC), established as part of the Energy Materials Network under the U.S. Department of Energy (DOE), Office of Energy Efficiency and Renewable Energy (EERE), Hydrogen and Fuel Cell Technologies Office (HFTO), under Contract No. DE-AC02-05CH11231 with Lawrence Berkeley National Laboratory. Single-crystal X-ray diffraction data were collected at beamlines 12.2.1 of the Advanced Light Source at Lawrence Berkeley National Laboratory, a user facility supported by the U.S. DOE, Office of Science under Contract No. DE-AC02-05CH11231. Nuclear magnetic resonance instruments in this work were supported by the Pines Magnetic Resonance Center's Core NMR Facility. Powder neutron diffraction and inelastic neutron scattering measurements were performed at the High Flux Isotope Reactor (HFIR) and the Spallation Neutron Source (SNS), a DOE Office of Science User Facility operated by the Oak Ridge National Laboratory. Powder synchrotron X-ray diffraction data were collected on the 17-BM-B at the Advanced Photon Source, a DOE Office of Science user facility operated for the DOE Office of Science by Argonne National Laboratory under Contract No. DE-AC02-06CH11357. We thank Dr. Henry Z. H. Jiang for helpful discussions with *in situ* gas-dosing infrared spectroscopy measurements, Dr. Andrey Yakovenko, Dr. Wenqian Xu, and Dr. Benjamin Trump for assistance with powder X-ray diffraction measurements, Dr. Tanya Dax, Dr. Mark Loguillo, Dr. Anibal "Timmy" Ramirez-Cuesta, and the sample environment, health physics, and diffraction teams at the SNS and HFIR for technical assistance, Dr. Hasan Celik, Dr. Raynald Giovine, and the Core NMR Facility of the Pines Magnetic Resonance Center for assistance with NMR measurements, and Dr. Matthew N. Dods and Hyunchul Kwon for helpful discussions. K.M.C. is supported by an Arnold O. Beckman postdoctoral fellowship. R.A.K. gratefully acknowledges support from the U.S. DOE, Office of EERE, HFTO under Contract No. DE-AC36-8GO28308 to the National Renewable Energy Laboratory.

■ REFERENCES

(1) Turner, J. A. Sustainable Hydrogen Production. *Science* **2004**, *305* (5686), 972−974.

(2) Megía, P. J.; Vizcaíno, A. J.; Calles, J. A.; Carrero, A. Hydrogen Production Technologies: From Fossil Fuels toward Renewable Sources. A Mini Review. *Energy Fuels* **2021**, *35* (20), 16403−16415.

(3) Barthelemy, H.; Weber, M.; Barbier, F. Hydrogen Storage: Recent Improvements and Industrial Perspectives. *Int. J. Hydrogen Energy* **2017**, *42* (11), 7254−7262.

(4) Allendorf, M. D.; Hulvey, Z.; Gennett, T.; Ahmed, A.; Autrey, T.; Camp, J.; Seon Cho, E.; Furukawa, H.; Haranczyk, M.; Head-Gordon, M.; Jeong, S.; Karkamkar, A.; Liu, D.-J.; Long, J. R.; Meihaus, K. R.; Nayyar, I. H.; Nazarov, R.; Siegel, D. J.; Stavila, V.; Urban, J. J.; Veccham, S. P.; Wood, B. C. An Assessment of Strategies for the Development of Solid-State Adsorbents for Vehicular Hydrogen Storage. *Energy Environ. Sci.* **2018**, *11* (10), 2784−2812.

(5) Rusman, N. A. A.; Dahari, M. A Review on the Current Progress of Metal Hydrides Material for Solid-State Hydrogen Storage Applications. *Int. J. Hydrogen Energy* **2016**, *41* (28), 12108−12126.

(6) Preuster, P.; Papp, C.; Wasserscheid, P. Liquid Organic Hydrogen Carriers (LOHCs): Toward a Hydrogen-Free Hydrogen Economy. *Acc. Chem. Res.* **2017**, *50* (1), 74−85.

(7) He, T.; Pachfule, P.; Wu, H.; Xu, Q.; Chen, P. Hydrogen Carriers. *Nat. Rev. Mater.* **2016**, *1* (12), No. 16059.

(8) Suh, M. P.; Park, H. J.; Prasad, T. K.; Lim, D.-W. Hydrogen Storage in Metal−Organic Frameworks. *Chem. Rev.* **2012**, *112* (2), 782−835.

(9) Furukawa, H.; Cordova, K. E.; O'Keeffe, M.; Yaghi, O. M. The Chemistry and Applications of Metal−Organic Frameworks. *Science* **2013**, *341* (6149), No. 1230444.

(10) Klein, N.; Senkovska, I.; Gedrich, K.; Stoeck, U.; Henschel, A.; Mueller, U.; Kaskel, S. A Mesoporous Metal−Organic Framework. *Angew. Chem., Int. Ed.* **2009**, *48* (52), 9954−9957.

(11) Furukawa, H.; Ko, N.; Go, Y. B.; Aratani, N.; Choi, S. B.; Choi, E.; Yazaydin, A. O.; Snurr, R. Q.; O'Keeffe, M.; Kim, J.; Yaghi, O. M. Ultrahigh Porosity in Metal−Organic Frameworks. *Science* **2010**, *329* (5990), 424−428.

(12) Yuan, D.; Zhao, D.; Sun, D.; Zhou, H. An Isoreticular Series of Metal−Organic Frameworks with Dendritic Hexacarboxylate Ligands and Exceptionally High Gas-Uptake Capacity. *Angew. Chem., Int. Ed.* **2010**, *49* (31), 5357−5361.

(13) Chen, Z.; Li, P.; Anderson, R.; Wang, X.; Zhang, X.; Robison, L.; Redfern, L. R.; Moribe, S.; Islamoglu, T.; Gómez-Gualdrón, D. A.; Yildirim, T.; Stoddart, J. F.; Farha, O. K. Balancing Volumetric and Gravimetric Uptake in Highly Porous Materials for Clean Energy. *Science* **2020**, *368* (6488), 297−303.

(14) Lin, R.-B.; Xiang, S.; Xing, H.; Zhou, W.; Chen, B. Exploration of Porous Metal−Organic Frameworks for Gas Separation and Purification. *Coord. Chem. Rev.* **2019**, *378*, 87−103.

(15) Bae, Y.-S.; Snurr, R. Q. Optimal Isosteric Heat of Adsorption for Hydrogen Storage and Delivery Using Metal−Organic Frameworks. *Microporous Mesoporous Mater.* **2010**, *132* (1−2), 300−303.
(16) Peng, P.; Anastasopoulou, A.; Brooks, K.; Furukawa, H.; Bowden, M. E.; Long, J. R.; Autrey, T.; Breunig, H. Cost and Potential of Metal−Organic Frameworks for Hydrogen Back-up Power Supply. *Nat. Energy* **2022**, *7* (5), 448−458.
(17) Bhatia, S. K.; Myers, A. L. Optimum Conditions for Adsorptive Storage. *Langmuir* **2006**, *22* (4), 1688−1700.
(18) Areán, C. O.; Chavan, S.; Cabello, C. P.; Garrone, E.; Palomino, G. T. Thermodynamics of Hydrogen Adsorption on Metal−Organic Frameworks. *ChemPhysChem* **2010**, *11* (15), 3237−3242.
(19) Rowsell, J. L. C.; Yaghi, O. M. Effects of Functionalization, Catenation, and Variation of the Metal Oxide and Organic Linking Units on the Low-Pressure Hydrogen Adsorption Properties of Metal−Organic Frameworks. *J. Am. Chem. Soc.* **2006**, *128* (4), 1304−1315.
(20) Zhang, Y.-B.; Furukawa, H.; Ko, N.; Nie, W.; Park, H. J.; Okajima, S.; Cordova, K. E.; Deng, H.; Kim, J.; Yaghi, O. M. Introduction of Functionality, Selection of Topology, and Enhancement of Gas Adsorption in Multivariate Metal−Organic Framework-177. *J. Am. Chem. Soc.* **2015**, *137* (7), 2641−2650.
(21) Chen, B.; Zhao, X.; Putkham, A.; Hong, K.; Lobkovsky, E. B.; Hurtado, E. J.; Fletcher, A. J.; Thomas, K. M. Surface Interactions and Quantum Kinetic Molecular Sieving for H_2 and D_2 Adsorption on a Mixed Metal−Organic Framework Material. *J. Am. Chem. Soc.* **2008**, *130* (20), 6411−6423.
(22) Mulfort, K. L.; Hupp, J. T. Chemical Reduction of Metal−Organic Framework Materials as a Method to Enhance Gas Uptake and Binding. *J. Am. Chem. Soc.* **2007**, *129* (31), 9604−9605.
(23) Chen, B.; Ockwig, N. W.; Millward, A. R.; Contreras, D. S.; Yaghi, O. M. High H_2 Adsorption in a Microporous Metal−Organic Framework with Open Metal Sites. *Angew. Chem., Int. Ed.* **2005**, *44* (30), 4745−4749.
(24) Dietzel, P. D. C.; Panella, B.; Hirscher, M.; Blom, R.; Fjellvåg, H. Hydrogen Adsorption in a Nickel Based Coordination Polymer with Open Metal Sites in the Cylindrical Cavities of the Desolvated Framework. *Chem. Commun.* **2006**, *1* (9), 959−961.
(25) Zhou, W.; Wu, H.; Yildirim, T. Enhanced H_2 Adsorption in Isostructural Metal−Organic Frameworks with Open Metal Sites: Strong Dependence of the Binding Strength on Metal Ions. *J. Am. Chem. Soc.* **2008**, *130* (46), 15268−15269.
(26) Sumida, K.; Stück, D.; Mino, L.; Chai, J.-D.; Bloch, E. D.; Zavorotynska, O.; Murray, L. J.; Dincă, M.; Chavan, S.; Bordiga, S.; Head-Gordon, M.; Long, J. R. Impact of Metal and Anion Substitutions on the Hydrogen Storage Properties of M-BTT Metal−Organic Frameworks. *J. Am. Chem. Soc.* **2013**, *135* (3), 1083−1091.
(27) Kapelewski, M. T.; Geier, S. J.; Hudson, M. R.; Stück, D.; Mason, J. A.; Nelson, J. N.; Xiao, D. J.; Hulvey, Z.; Gilmour, E.; FitzGerald, S. A.; Head-Gordon, M.; Brown, C. M.; Long, J. R. M_2(*m*-dobdc) (M = Mg, Mn, Fe, Co, Ni) Metal−Organic Frameworks Exhibiting Increased Charge Density and Enhanced H_2 Binding at the Open Metal Sites. *J. Am. Chem. Soc.* **2014**, *136* (34), 12119−12129.
(28) Tsivion, E.; Long, J. R.; Head-Gordon, M. Hydrogen Physisorption on Metal−Organic Framework Linkers and Metalated Linkers: A Computational Study of the Factors That Control Binding Strength. *J. Am. Chem. Soc.* **2014**, *136* (51), 17827−17835.
(29) Gygi, D.; Bloch, E. D.; Mason, J. A.; Hudson, M. R.; Gonzalez, M. I.; Siegelman, R. L.; Darwish, T. A.; Queen, W. L.; Brown, C. M.; Long, J. R. Hydrogen Storage in the Expanded Pore Metal−Organic Frameworks M_2(dobpdc) (M = Mg, Mn, Fe, Co, Ni, Zn). *Chem. Mater.* **2016**, *28* (4), 1128−1138.
(30) Oppenheim, J. J.; Mancuso, J. L.; Wright, A. M.; Rieth, A. J.; Hendon, C. H.; Dincă, M. Divergent Adsorption Behavior Controlled by Primary Coordination Sphere Anions in the Metal−Organic Framework Ni_2X_2BTDD. *J. Am. Chem. Soc.* **2021**, *143* (40), 16343−16347.
(31) Irving, H.; Williams, R. J. P. The Stability of Transition-Metal Complexes. *J. Chem. Soc.* **1953**, 3192−3210.
(32) Kapelewski, M. T.; Runčevski, T.; Tarver, J. D.; Jiang, H. Z. H.; Hurst, K. E.; Parilla, P. A.; Ayala, A.; Gennett, T.; FitzGerald, S. A.; Brown, C. M.; Long, J. R. Record High Hydrogen Storage Capacity in the Metal−Organic Framework Ni_2(*m*-dobdc) at Near-Ambient Temperatures. *Chem. Mater.* **2018**, *30* (22), 8179−8189.
(33) Lee, K.; Isley, W. C.; Dzubak, A. L.; Verma, P.; Stoneburner, S. J.; Lin, L.-C.; Howe, J. D.; Bloch, E. D.; Reed, D. A.; Hudson, M. R.; Brown, C. M.; Long, J. R.; Neaton, J. B.; Smit, B.; Cramer, C. J.; Truhlar, D. G.; Gagliardi, L. Design of a Metal−Organic Framework with Enhanced Back Bonding for Separation of N_2 and CH_4. *J. Am. Chem. Soc.* **2014**, *136* (2), 698−704.
(34) Jaramillo, D. E.; Reed, D. A.; Jiang, H. Z. H.; Oktawiec, J.; Mara, M. W.; Forse, A. C.; Lussier, D. J.; Murphy, R. A.; Cunningham, M.; Colombo, V.; Shuh, D. K.; Reimer, J. A.; Long, J. R. Selective Nitrogen Adsorption via Backbonding in a Metal−Organic Framework with Exposed Vanadium Sites. *Nat. Mater.* **2020**, *19* (5), 517−521.
(35) Jaramillo, D. E.; Jiang, H. Z. H.; Evans, H. A.; Chakraborty, R.; Furukawa, H.; Brown, C. M.; Head-Gordon, M.; Long, J. R. Ambient-Temperature Hydrogen Storage via Vanadium(II)-Dihydrogen Complexation in a Metal−Organic Framework. *J. Am. Chem. Soc.* **2021**, *143* (16), 6248−6256.
(36) Liao, P.; Li, X.; Bai, J.; He, C.; Zhou, D.; Zhang, W.; Zhang, J.; Chen, X. Drastic Enhancement of Catalytic Activity via Post-Oxidation of a Porous Mn^{II} Triazolate Framework. *Chem.—Eur. J.* **2014**, *20* (36), 11303−11307.
(37) Liao, P.-Q.; Chen, H.; Zhou, D.-D.; Liu, S.-Y.; He, C.-T.; Rui, Z.; Ji, H.; Zhang, J.-P.; Chen, X.-M. Monodentate Hydroxide as a Super Strong yet Reversible Active Site for CO_2 Capture from High-Humidity Flue Gas. *Energy Environ. Sci.* **2015**, *8* (3), 1011−1016.
(38) Rosi, N. L.; Kim, J.; Eddaoudi, M.; Chen, B.; O'Keeffe, M.; Yaghi, O. M. Rod Packings and Metal−Organic Frameworks Constructed from Rod-Shaped Secondary Building Units. *J. Am. Chem. Soc.* **2005**, *127* (5), 1504−1518.
(39) Dietzel, P. D. C.; Morita, Y.; Blom, R.; Fjellvåg, H. An *in Situ* High-Temperature Single-Crystal Investigation of a Dehydrated Metal−Organic Framework Compound and Field-Induced Magnetization of One-Dimensional Metal−Oxygen Chains. *Angew. Chem., Int. Ed.* **2005**, *44* (39), 6354−6358.
(40) Denysenko, D.; Grzywa, M.; Jelic, J.; Reuter, K.; Volkmer, D. Scorpionate-Type Coordination in MFU-4*l* Metal−Organic Frameworks: Small-Molecule Binding and Activation upon the Thermally Activated Formation of Open Metal Sites. *Angew. Chem., Int. Ed.* **2014**, *53* (23), 5832−5836.
(41) Barnett, B. R.; Evans, H. A.; Su, G. M.; Jiang, H. Z. H.; Chakraborty, R.; Banyeretse, D.; Hartman, T. J.; Martinez, M. B.; Trump, B. A.; Tarver, J. D.; Dods, M. N.; Funke, L. M.; Börgel, J.; Reimer, J. A.; Drisdell, W. S.; Hurst, K. E.; Gennett, T.; FitzGerald, S. A.; Brown, C. M.; Head-Gordon, M.; Long, J. R. Observation of an Intermediate to H_2 Binding in a Metal−Organic Framework. *J. Am. Chem. Soc.* **2021**, *143* (36), 14884−14894.
(42) Schmieder, P.; Denysenko, D.; Grzywa, M.; Magdysyuk, O.; Volkmer, D. A Structurally Flexible Triazolate-Based Metal−Organic Framework Featuring Coordinatively Unsaturated Copper(I) Sites. *Dalton Trans.* **2016**, *45* (35), 13853−13862.
(43) Fritzsche, J.; Denysenko, D.; Grzywa, M.; Volkmer, D. CFA-13 − a Bifunctional Perfluorinated Metal−Organic Framework Featuring Active Cu(I) and Cu(II) Sites. *Dalton Trans.* **2017**, *46* (43), 14907−14915.
(44) Sengupta, D.; Melix, P.; Bose, S.; Duncan, J.; Wang, X.; Mian, M. R.; Kirlikovali, K. O.; Joodaki, F.; Islamoglu, T.; Yildirim, T.; Snurr, R. Q.; Farha, O. K. Air-Stable Cu(I) Metal−Organic Framework for Hydrogen Storage. *J. Am. Chem. Soc.* **2023**, *145* (37), 20492−20502.
(45) Companion, A. L.; Komarynsky, M. A. Crystal Field Splitting Diagrams. *J. Chem. Educ.* **1964**, *41* (5), 257−262.

(46) Denysenko, D.; Grzywa, M.; Tonigold, M.; Streppel, B.; Krkljus, I.; Hirscher, M.; Mugnaioli, E.; Kolb, U.; Hanss, J.; Volkmer, D. Elucidating Gating Effects for Hydrogen Sorption in MFU-4-Type Triazolate-Based Metal−Organic Frameworks Featuring Different Pore Sizes. *Chem.—Eur. J.* **2011**, *17* (6), 1837−1848.
(47) Schmieder, P.; Denysenko, D.; Grzywa, M.; Baumgärtner, B.; Senkovska, I.; Kaskel, S.; Sastre, G.; van Wüllen, L.; Volkmer, D. CFA-1: The First Chiral Metal−Organic Framework Containing Kuratowski-Type Secondary Building Units. *Dalton Trans.* **2013**, *42* (30), 10786−10797.
(48) Schmieder, P.; Grzywa, M.; Denysenko, D.; Hambach, M.; Volkmer, D. **CFA-7**: An Interpenetrated Metal−Organic Framework of the MFU-4 Family. *Dalton Trans.* **2015**, *44* (29), 13060−13070.
(49) Denysenko, D.; Jelic, J.; Reuter, K.; Volkmer, D. Postsynthetic Metal and Ligand Exchange in MFU-4*l*: A Screening Approach toward Functional Metal−Organic Frameworks Comprising Single-Site Active Centers. *Chem.—Eur. J.* **2015**, *21* (22), 8188−8199.
(50) Alezi, D.; Oppenheim, J. J.; Sarver, P. J.; Iliescu, A.; Dinakar, B.; Dincă, M. Tunable Low−Relative Humidity and High−Capacity Water Adsorption in a Bibenzotriazole Metal−Organic Framework. *J. Am. Chem. Soc.* **2023**, *145* (46), 25233−25241.
(51) Denysenko, D.; Werner, T.; Grzywa, M.; Puls, A.; Hagen, V.; Eickerling, G.; Jelic, J.; Reuter, K.; Volkmer, D. Reversible Gas-Phase Redox Processes Catalyzed by Co-Exchanged MFU-4*l*(arge). *Chem. Commun.* **2012**, *48* (9), 1236−1238.
(52) Shannon, R. D. Revised Effective Ionic Radii and Systematic Studies of Interatomic Distances in Halides and Chalcogenides. *Acta Crystallogr., Sect. A* **1976**, *32* (5), 751−767.
(53) Rieth, A. J.; Tulchinsky, Y.; Dincă, M. High and Reversible Ammonia Uptake in Mesoporous Azolate Metal−Organic Frameworks with Open Mn, Co, and Ni Sites. *J. Am. Chem. Soc.* **2016**, *138* (30), 9401−9404.
(54) Reed, D. A.; Keitz, B. K.; Oktawiec, J.; Mason, J. A.; Runčevski, T.; Xiao, D. J.; Darago, L. E.; Crocellà, V.; Bordiga, S.; Long, J. R. A Spin Transition Mechanism for Cooperative Adsorption in Metal−Organic Frameworks. *Nature* **2017**, *550* (7674), 96−100.
(55) Sing, K. S. W.; Rouquerol, F.; Llewellyn, P.; Rouquerol, J. Assessment of Microporosity. In *Adsorption by Powders and Porous Solids*; Elsevier, 2014; pp 303−320 DOI: 10.1016/B978-0-08-097035-6.00009-7.
(56) Connolly, M. L. Computation of Molecular Volume. *J. Am. Chem. Soc.* **1985**, *107* (5), 1118−1124.
(57) Hou, K.; Börgel, J.; Jiang, H. Z. H.; SantaLucia, D. J.; Kwon, H.; Zhuang, H.; Chakarawet, K.; Rohde, R. C.; Taylor, J. W.; Dun, C.; Paley, M. V.; Turkiewicz, A. B.; Park, J. G.; Mao, H.; Zhu, Z.; Alp, E. E.; Zhao, J.; Hu, M. Y.; Lavina, B.; Peredkov, S.; Lv, X.; Oktawiec, J.; Meihaus, K. R.; Pantazis, D. A.; Vandone, M.; Colombo, V.; Bill, E.; Urban, J. J.; Britt, R. D.; Grandjean, F.; Long, G. J.; DeBeer, S.; Neese, F.; Reimer, J. A.; Long, J. R. Reactive High-Spin Iron(IV)-Oxo Sites through Dioxygen Activation in a Metal−Organic Framework. *Science* **2023**, *382* (6670), 547−553.
(58) Carsch, K. M.; Huang, A. J.; Dods, M. N.; Parker, S. T.; Rohde, R. C.; Jiang, H. Z. H.; Yabuuchi, Y.; Karstens, S. L.; Kwon, H.; Chakraborty, R.; Bustillo, K. C.; Meihaus, K. R.; Furukawa, H.; Minor, A. M.; Head-Gordon, M.; Long, J. R. Selective Adsorption of Oxygen from Humid Air in a Metal−Organic Framework with Trigonal Pyramidal Copper(I) Sites. *J. Am. Chem. Soc.* **2024**, *146* (5), 3160−3170.
(59) Thommes, M.; Kaneko, K.; Neimark, A. V.; Olivier, J. P.; Rodriguez-Reinoso, F.; Rouquerol, J.; Sing, K. S. W. Physisorption of Gases, with Special Reference to the Evaluation of Surface Area and Pore Size Distribution (IUPAC Technical Report). *Pure Appl. Chem.* **2015**, *87* (9−10), 1051−1069.
(60) Nuhnen, A.; Janiak, C. A Practical Guide to Calculate the Isosteric Heat/Enthalpy of Adsorption *via* Adsorption Isotherms in Metal−Organic Frameworks, MOFs. *Dalton Trans.* **2020**, *49* (30), 10295−10307.
(61) Huang, Y. The Temperature Dependence of Isosteric Heat of Adsorption on the Heterogeneous Surface. *J. Catal.* **1972**, *25* (1), 131−138.
(62) Hyla, A. S.; Fang, H.; Boulfelfel, S. E.; Muraro, G.; Paur, C.; Strohmaier, K.; Ravikovitch, P. I.; Sholl, D. S. Significant Temperature Dependence of the Isosteric Heats of Adsorption of Gases in Zeolites Demonstrated by Experiments and Molecular Simulations. *J. Phys. Chem. C* **2019**, *123* (33), 20405−20412.
(63) Rahman, K. A.; Loh, W. S.; Ng, K. C. Heat of Adsorption and Adsorbed Phase Specific Heat Capacity of Methane/Activated Carbon System. *Procedia Eng.* **2013**, *56*, 118−125.
(64) Stoicheff, B. P. High Resolution Raman Spectroscopy of Gases: IX. Spectra of H_2, HD, and D_2. *Can. J. Phys.* **1957**, *35* (6), 730−741.
(65) Bender, B. R.; Kubas, G. J.; Jones, L. H.; Swanson, B. I.; Eckert, J.; Capps, K. B.; Hoff, C. D. Why Does D_2 Bind Better than H_2? A Theoretical and Experimental Study of the Equilibrium Isotope Effect on H_2 Binding in a M(η^2-H_2) Complex. Normal Coordinate Analysis of $W(CO)_3(PCy_3)_2(\eta^2\text{-}H_2)$. *J. Am. Chem. Soc.* **1997**, *119* (39), 9179−9190.
(66) Weinrauch, I.; Savchenko, I.; Denysenko, D.; Souliou, S. M.; Kim, H.-H.; Le Tacon, M.; Daemen, L. L.; Cheng, Y.; Mavrandonakis, A.; Ramirez-Cuesta, A. J.; Volkmer, D.; Schütz, G.; Hirscher, M.; Heine, T. Capture of Heavy Hydrogen Isotopes in a Metal−Organic Framework with Active Cu(I) Sites. *Nat. Commun.* **2017**, *8* (1), No. 14496.
(67) *American Institute of Physics Handbook: Section Eds.: Bruce H. Billings [and others] Coordinating Ed.: Dwight E. Gray*; Billings, B. J.; Gray, D. E., Eds.; McGraw-Hill, 1972.
(68) Chakraborty, R.; Talbot, J. J.; Shen, H.; Yabuuchi, Y.; Carsch, K. M.; Jiang, H. Z. H.; Furukawa, H.; Long, J. R.; Head-Gordon, M. Quantum Chemical Modeling of Hydrogen Binding in Metal−Organic Frameworks: Validation, Insight, Predictions and Challenges. *Phys. Chem. Chem. Phys.* **2024**, *26* (8), 6490−6511.
(69) Khaliullin, R. Z.; Cobar, E. A.; Lochan, R. C.; Bell, A. T.; Head-Gordon, M. Unravelling the Origin of Intermolecular Interactions Using Absolutely Localized Molecular Orbitals. *J. Phys. Chem. A* **2007**, *111* (36), 8753−8765.
(70) Horn, P. R.; Mao, Y.; Head-Gordon, M. Probing Non-Covalent Interactions with a Second Generation Energy Decomposition Analysis Using Absolutely Localized Molecular Orbitals. *Phys. Chem. Chem. Phys.* **2016**, *18* (33), 23067−23079.
(71) Levine, D. S.; Head-Gordon, M. Energy Decomposition Analysis of Single Bonds within Kohn−Sham Density Functional Theory. *Proc. Natl. Acad. Sci. U.S.A.* **2017**, *114* (48), 12649−12656.
(72) Sears, V. F. Neutron Scattering Lengths and Cross Sections. *Neutron News* **1992**, *3* (3), 26−37.
(73) Brown, C. M.; Liu, Y.; Yildirim, T.; Peterson, V. K.; Kepert, C. J. Hydrogen Adsorption in HKUST-1: A Combined Inelastic Neutron Scattering and First-Principles Study. *Nanotechnology* **2009**, *20* (20), No. 204025.
(74) Eckert, J.; Kubas, G. J. Barrier to Rotation of the Dihydrogen Ligand in Metal Complexes. *J. Phys. Chem. A* **1993**, *97* (10), 2378−2384.
(75) Kong, L.; Román-Pérez, G.; Soler, J. M.; Langreth, D. C. Energetics and Dynamics of H_2 Adsorbed in a Nanoporous Material at Low Temperature. *Phys. Rev. Lett.* **2009**, *103* (9), No. 096103.
(76) Dietzel, P. D. C.; Georgiev, P. A.; Eckert, J.; Blom, R.; Strässle, T.; Unruh, T. Interaction of Hydrogen with Accessible Metal Sites in the Metal−Organic Frameworks M_2(dhtp) (CPO-27-M; M = Ni, Co, Mg). *Chem. Commun.* **2010**, *46* (27), 4962−4964.
(77) Mitchell, P. C. H. *Vibrational Spectroscopy with Neutrons: With Applications in Chemistry, Biology, Materials Science and Catalysis*; World Scientific, 2005.
(78) Sircar, S. Gibbsian Surface Excess for Gas Adsorption Revisited. *Ind. Eng. Chem. Res.* **1999**, *38* (10), 3670−3682.
(79) Myers, A. L.; Calles, J. A.; Calleja, G. Comparison of Molecular Simulation of Adsorption with Experiment. *Adsorption* **1997**, *3* (2), 107−115.

(80) Anastasopoulou, A.; Furukawa, H.; Barnett, B. R.; Jiang, H. Z. H.; Long, J. R.; Breunig, H. M. Technoeconomic Analysis of Metal−Organic Frameworks for Bulk Hydrogen Transportation. *Energy Environ. Sci.* **2021**, *14* (3), 1083−1094.
(81) Mason, J. A.; Veenstra, M.; Long, J. R. Evaluating Metal−Organic Frameworks for Natural Gas Storage. *Chem. Sci.* **2014**, *5* (1), 32−51.
(82) Runčevski, T.; Kapelewski, M. T.; Torres-Gavosto, R. M.; Tarver, J. D.; Brown, C. M.; Long, J. R. Adsorption of Two Gas Molecules at a Single Metal Site in a Metal−Organic Framework. *Chem. Commun.* **2016**, *52* (53), 8251−8254.
(83) Sumida, K.; Brown, C. M.; Herm, Z. R.; Chavan, S.; Bordiga, S.; Long, J. R. Hydrogen Storage Properties and Neutron Scattering Studies of Mg_2(dobdc)—a Metal−Organic Framework with Open Mg^{2+} Adsorption Sites. *Chem. Commun.* **2011**, *47* (4), 1157−1159.
(84) Röß-Ohlenroth, R.; Kraft, M.; Bunzen, H.; Volkmer, D. Inhibition, Binding of Organometallics, and Thermally Induced CO Release in an MFU-4-Type Metal−Organic Framework Scaffold with Open Bidentate Bibenzimidazole Coordination Sites. *Inorg. Chem.* **2022**, *61* (41), 16380−16389.
(85) Tranchemontagne, D. J.; Mendoza-Cortés, J. L.; O'Keeffe, M.; Yaghi, O. M. Secondary Building Units, Nets and Bonding in the Chemistry of Metal−Organic Frameworks. *Chem. Soc. Rev.* **2009**, *38* (5), 1257−1283.
(86) Bacquart, T.; Murugan, A.; Carré, M.; Gozlan, B.; Auprêtre, F.; Haloua, F.; Aarhaug, T. A. Probability of Occurrence of ISO 14687−2 Contaminants in Hydrogen: Principles and Examples from Steam Methane Reforming and Electrolysis (Water and Chlor-Alkali) Production Processes Model. *Int. J. Hydrogen Energy* **2018**, *43* (26), 11872−11883.

https://doi.org/10.1021/jacs.4c08039
J. Am. Chem. Soc. 2024, 146, 22759−22776